nature communications

Article

https://doi.org/10.1038/s41467-024-53970-3

Endocytosis restricts dendrite branching via removing ectopically localized branching ligands

Received: 19 October 2023

Accepted: 26 October 2024

Jie Fang[1,2,3,6], Wenli Jiang[4,5,6], Weixia Zhao[1,2,6], Jie Wang[1,2], Beibei Cao[1,2], Nan Wang[1,2], Baohui Chen[3], Chao Wang[4,5] ✉ & Wei Zou[1,2] ✉

Neurons often grow highly branched and cell-type specific dendrite morphologies to receive and integrate information, which is the basis of precise neural circuit formation. Previous studies have identified numerous mechanisms that promote dendrite branching. In contrast, it is much less understood how this process is negatively regulated. Here we show that EAT-17/EVI5 acts together with the dynein adaptor protein BICD-1 and the motor protein dynein in *C. elegans* epidermal cells to restrict branching of PVD sensory dendrites. Loss-of-function mutants of these genes cause both ectopic branching and accumulation of the dendrite branching ligand SAX-7/L1CAM on epidermal plasma membranes. Mutants of genes regulating endo-lysosomal trafficking, including *rab-5/RAB5* and *dyn-1/DNM1*, show similar defects. Biochemical characterization, genetic analysis, and imaging results support that EAT-17 and BICD-1 directly interact with each other and function in the endocytic degradation pathway to remove ectopically localized dendrite branching ligands to restrict abnormal branching.

Neurons form cell-type-specific dendrite morphologies to receive and integrate signaling input, which is pivotal for precise neural circuit assembly. Previous studies have identified numerous intrinsic and extrinsic regulators required for dendrite branching and outgrowth. Intrinsic regulators include transcription factors, endocytosis and secretory pathways, motor proteins and cytoskeletal regulators. Extrinsic regulators are mainly secreted molecules and environment-localized cell adhesion proteins, which can be recognized by dendrite surface-localized receptors to guide dendritic branching and outgrowth. Knockout of most of the abovementioned regulators often causes reduced dendrite branching, suggesting that most of them are positive regulators[1–5].

A few studies identified several negative regulators. First, RhoA GTPase acts as a negative regulator of dendrite development by modulating the actin cytoskeleton[6]. Second, Rho 1 and the Rho GEF Trio function downstream of the Wnt5-Drl signaling pathway to promote dendrite termination in adult *Drosophila*[7]. In the mammalian system, reduced expression of the Wnt receptor Ryk in the mouse hippocampus and cortex leads to excessive dendrite outgrowth and branching both in vitro and in vivo[8]. Third, the Tricornered-Kinase/Furry pathway restricts dendrite branching via negatively regulating Rac signaling[9]. However, despite significant advancements in our understanding of the positive regulation of dendrite branching, the mechanisms involved in its negative regulation remain relatively unclear.

To identify negative regulators of dendrite branching, we used the *C. elegans* multi-dendritic PVD neuron as a model. Each animal grows two PVD neurons to cover ~80% of the body surface (except the head and neck regions), namely PVDL and PVDR, which are on the left and

---

[1]The Fourth Affiliated Hospital, Zhejiang University School of Medicine, Yiwu, China. [2]Institute of Translational Medicine, Zhejiang University, Hangzhou, China. [3]Department of Cell Biology, and Bone Marrow Transplantation Center of the First Affiliated Hospital, Zhejiang University School of Medicine, Hangzhou, China. [4]MOE Key Laboratory for Membraneless Organelles & Cellular Dynamics, Hefei National Research Center for Physical Sciences at the Microscale, Biomedical Sciences and Health Laboratory of Anhui Province, School of Life Sciences, Division of Life Sciences and Medicine, University of Science and Technology of China, Hefei, China. [5]Department of Neurology, the First Affiliated Hospital of USTC, Division of Life Sciences and Medicine, University of Science and Technology of China, Hefei, China. [6]These authors contributed equally: Jie Fang, Wenli Jiang, Weixia Zhao.
✉e-mail: cwangust@ustc.edu.cn; zouwei@zju.edu.cn

right sides, respectively. PVD neurons are born at the second larval stage (L2), and grow two primary (1°) dendrites along the anterior-posterior axis. At the late L2 and early third larval (L3) stages, numerous secondary (2°) branches grow toward either the dorsal or the ventral side. Later, when the 2° branches reach the border of the outer body wall muscles, they form "T" shaped tertiary (3°) branches. At the early fourth larval (L4) stage, quaternary branches are formed perpendicularly to the 3° branches and sandwiched by the epidermis and body wall muscle cells (Fig. 1a, b)[10].

Previous studies by others and us have shown that the dendrite guidance and branching decisions are precisely controlled by a receptor-ligand complex, including a co-ligand complex formed by epidermis-localized SAX-7/L1CAM, MNR-1/Menorin and muscle-derived LECT-2/LECT2, and the dendritic receptor DMA-1/LRRTM[11–15]. In addition, HPO-30 acts as a signaling co-organizer of the DMA-1 receptor. Both DMA-1 and HPO-30 use their cytosolic tails to recruit or activate downstream actin assembly regulators to promote dendrite branching[16–18]. The cell-surface localization of DMA-1 relies on the RAB-10-exocyst-dependent membrane transport machinery and the IRE-1-dependent unfolded protein response pathway and is negatively regulated by KPC-1/Furin[19–23]. Loss-of-function mutants of the above-mentioned genes show reduced dendrite branching defects, supporting the notion that they are positive regulators of dendrite branching and/or stabilization. Notably, the dendrite branching ligand SAX-7 is a type I transmembrane protein that is enriched in the dorsal and ventral muscle regions to provide spatial information to guide dendrite innervation onto the body wall muscles. In contrast, its level on the lateral epidermal region is relatively low (except the epidermis-seam cell junctions) (Fig. 1b)[11,23,24]. It is currently unknown how SAX-7 forms such a "muscle region high and lateral region low" pattern.

In this study, we find that EAT-17, the *C. elegans* homolog of Ecotropic Viral Integration Site 5 (EVI5), functions in the epidermis to restrict dendrite branching in the lateral region. Mechanistically, EAT-17 acts together with the dynein adaptor protein BICD-1 and the motor protein dynein to promote endocytosis of the ectopically localized branching ligand SAX-7 on the lateral epidermis to prevent ectopic dendrite branching. Since most of the regulators we identified are evolutionarily conserved from worms to humans, we propose that a similar mechanism might be used to restrict dendrite branching in humans.

Results

EAT-17 can regulate PVD dendrite morphogenesis independent of its RAB GTPase activating protein function

Previously, we and others found that the small GTPase RAB-10 functions cell-autonomously in the PVD neurons to promote dendrite branching and growth[19,20]. Since EAT-17 (also known as TBC-4) was reported to act as the GTPase-activating protein (GAP) of RAB-10, we sought to determine whether EAT-17 is required for proper dendrite development[25]. A previous study generated a full-length transcriptome of *C. elegans* by using nanopore-based direct RNA sequencing and showed that there are six isoforms of *eat-17*, including four long isoforms (*eat-17a*, *eat-17b*, *eat-17d* and *eat-17e*) and two short isoforms (*eat-17c* and *eat-17f*)[26,27]. Protein domain prediction revealed that the long isoforms generate proteins with a TBC domain and three coiled-coil domains, while the short isoforms generate proteins only with the last two coiled-coil domains (Fig. 1c, d)[28]. Since all six isoforms share the same C-terminal end, we inserted the coding sequence of the green fluorescent protein (GFP) before the stop codon and generated an *eat-17::gfp* knock-in strain using CRISPR-based homologous recombination[29]. Western blotting results confirmed that both long and short isoforms exist (Fig. 1e). We identified two RNAi clones in the Ahringer RNAi library: clone 201F11 contained a genomic fragment corresponding to most of the TBC domain, while clone 201F10 contained a genomic DNA segment corresponding to the C-terminal coiled-coil domains (CC2 and CC3). Knockdown of all *eat-17* isoforms using the 201F10 clone caused ectopic branch formation in the lateral region and decreased the number of 4° branches in the muscle regions. However, specific knockdown of *eat-17* long isoforms using the 201F11 clone did not cause any obvious defect (Fig. 1f–i), indicating that the short isoform(s) of *eat-17* is sufficient for proper dendrite branching.

To validate the results of the knockdown experiments, we conducted an analysis using three *eat-17* deletion mutants. *ok2983* is a deletion mutant affecting a portion of the 3′ half, while *ok2928* and *ok3041* impact different part of the 5′ half of the *eat-17* coding sequences. To understand how these mutations influence the expression of endogenous EAT-17 isoforms (both long and short), we introduced green fluorescent protein (GFP) to label these mutated proteins by genome editing. Western blotting results showed that *ok2983* completely abolishes expression of both EAT-17 long and short isoforms, whereas *ok2928* and *ok3041* specifically affects the EAT-17 long isoforms (Fig. 1e). Notably, the *ok2983* allele, which is presumed to be a null allele, generates a dendrite morphogenesis defect similar to that observed in animals treated with double-strand RNAs produced by the 201F10 clone. However, *ok2928* and *ok3041* displayed no obvious dendrite morphogenesis defect (Fig. 1f–i)[25]. We further used the CRISPR/Cas9-mediated genome editing to delete part of the 3′ half in *ok3041* and obtained *eat-17(zac305)* mutants, and we did not observe any enhanced defects in dendrite morphogenesis (Fig. 1f–i). Together, our results suggest that the *eat-17* short isoform(s) is sufficient to ensure proper dendrite morphogenesis.

Ectopic branch formation can be caused by increased branch initiation, decreased branch retraction, or both. To distinguish these possibilities, we performed time-lapse recordings for both wildtype and *eat-17(ok2983)* mutant animals at the young adult stage (~4 h post the fourth larval stage). We did not observe any significant difference for the speed of branch elongation or retraction (Fig. 2a–c). However, we observed more ectopic branch initiation (pointed by yellow arrows in Fig. 2a) and retraction (pointed by red arrows in Fig. 2a) events in *eat-17* mutants than in wildtype controls. The number of ectopic branch initiations was ~ 4 times higher than that of retractions, which explains why there were more ectopic branches in the *eat-17* mutants (Fig. 2d, e).

EAT-17 is expressed in the epidermis and functions at the third/fourth larval stage to inhibit ectopic branching

To understand in which tissue EAT-17 functions, we firstly analyzed the *eat-17::gfp* knock-in strain. Notably, this strain displayed normal PVD dendrite morphology, suggesting that C-terminal GFP tagging does not interfere with the function of endogenous EAT-17 (Supplementary Fig. 1a–d). We found that EAT-17::GFP was mainly expressed in the epidermis and seam cells and showed a diffused pattern in the cytosol (Fig. 3a). Consistently, the single-copy transgenes expressing EAT-17D::GFP (a long isoform) or EAT-17F::GFP (a short isoform), driven by an epidermis-specific promoter, mainly showed diffuse signals (Supplementary Fig. 2a). However, we could not exclude the possibility that EAT-17 might be expressed in other tissues at a level that is below the detection ability of our fluorescence microscopy. Previous studies revealed that PVD dendrite development mainly involves three tissues, the PVD neuron itself and the neighboring epidermis and body-wall muscles[2,4,5]. Thus, we expressed the cDNA of a short isoform of *eat-17* (*eat-17f*) using promoters that specifically drive transgene expression in the abovementioned tissues (*ser2prom3* for the PVD neuron, *hlh-1p* for the body wall muscles, and *dpy-7p* for the epidermis, respectively)[30–32]. Expressing EAT-17F in the epidermis rescued both the ectopic branching in the lateral region and the reduced branching in the dorsal and ventral muscle region of the *eat-17(ok2983)* mutants, while no rescue was observed when EAT-17F was expressed in the PVD neuron or the body-wall muscles (Fig. 3b–d). In addition, the dendrite

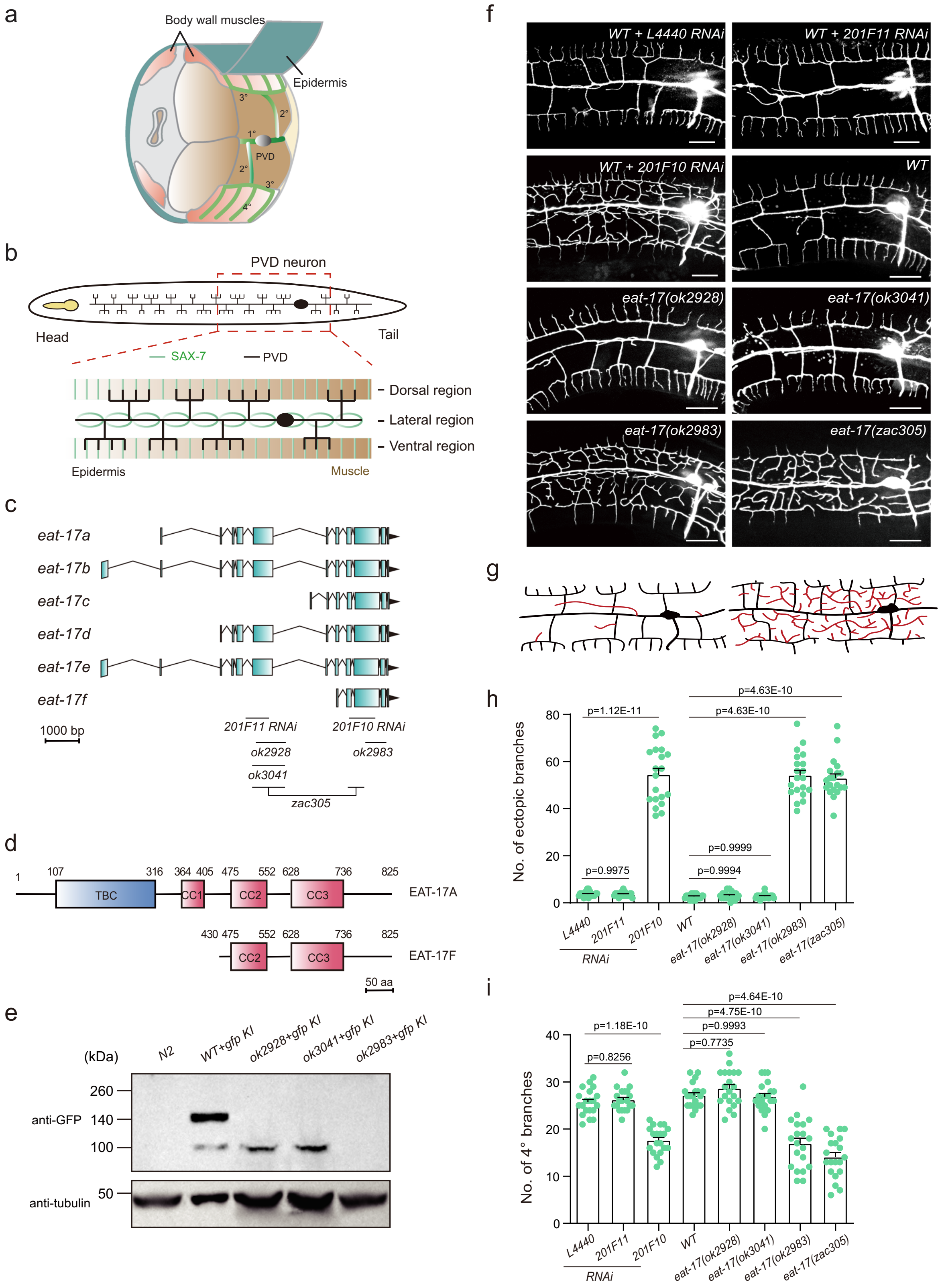

morphogenesis defects in *eat-17(ok2983)* mutants were rescued to a similar extent by the epidermis-specific expression of EAT-17A and EAT-17D isoforms (Supplementary Fig. 2b–d).

To explore when EAT-17 functions, we introduced a transgene (*hsp-16.48p::eat-17f* cDNA) in the *eat-17(ok2983)* mutants and induced EAT-17F expression at different developmental stages. For the ectopic branching defect, induction of EAT-17F expression at the L4 stage fully rescued the defect, and induction at the L3 stage also showed partial rescue. However, induction at the L1, L2, or 1 day post L4 stage failed to do so. Interestingly, for the reduced 4° branch formation defect, induction of EAT-17F expression at each abovementioned stage showed a full rescue (Fig. 3e–h). Together, our results showed that EAT-17 functions at the L3/L4 stage and in the epidermis to inhibit ectopic dendrite branching.

Fig. 1 | EAT-17 regulates dendrite morphogenesis independent of its Rab GAP activity. a A cartoon showing the morphology of the sensory PVD dendrites and the growth environment. Adapted from Zou et al. (2016)[14] with permission (https://creativecommons.org/licenses/by/4.0/). 1°: primary dendrite; 2°: secondary dendrite; 3°: tertiary dendrite; 4°: quaternary dendrite. Internal organs such as germline and intestine are inside of the pseudocoelom. **b** Schematic diagram showing that SAX-7 forms stripes in the dorsal and ventral muscle regions to guide the PVD branching. SAX-7's level is low in the lateral region, except the epidermal-seam cell junctions. **c** Schematic diagram of six isoforms of *eat-17* transcripts (adapted from Wormbase). The regions used to generate double-strand RNA and deleted in the deletion alleles are also shown. **d** Schematic diagram of EAT-17A (one of the four long isoforms) and EAT-17F (one of the two short isoforms). TBC: Tre2–Bub2–Cdc16 (TBC) domain (also known as the Rab GAP domain); CC: coiled-coil domain. **e** Western blotting results to show the molecular weight of endogenously expressed EAT-17::GFP in WT and different *eat-17* deletion mutant strains. The experiment was repeated 3 times with similar results. **f** Confocal images to show the PVD dendrite morphologies of wildtype animals treated with negative control L4440 (empty vector) RNAi, 201F11 RNAi (dsRNA targeting the 5′ half part of EAT-17), 201F10 (dsRNA targeting the 3′ half part of EAT-17) RNAi, and wildtype, *eat-17(ok2928)*, *eat-17(ok3041)*, *eat-17(ok2983)* and *eat-17(zac305)* mutant animals. The first three strains were fed with HT115 bacteria to knockdown target genes with specific double-stranded RNAs, and the last five strains were fed with regular food OP50 bacteria. All animals were at 1 day old adult stage (24 h post L4 stage). PVD dendrites were labeled using an integrated transgene *wyIs592* (*ser2prom3::myristoylated-gfp*). Scale bar, 20 µm. **g** Schematic diagram to show the dendrite morphologies of the 1 day old wildtype and *eat-17* mutant animals. Ectopic branches in the lateral region are showed in red. **h**, **i** Quantification of number of ectopic branches (**h**) and 4° branches (**i**) in a 100 µm region anterior to the PVD cell body for each strain showed in (**f**). All values are presented as mean ± s.e.m. $^{****}p < 0.0001$; ns: not significant (one-sided ANOVA with the Tukey correction). $n = 20$ 1 day old adult animals were quantified for each column. For (**e**–**i**). source data are provided as a Source Data file.

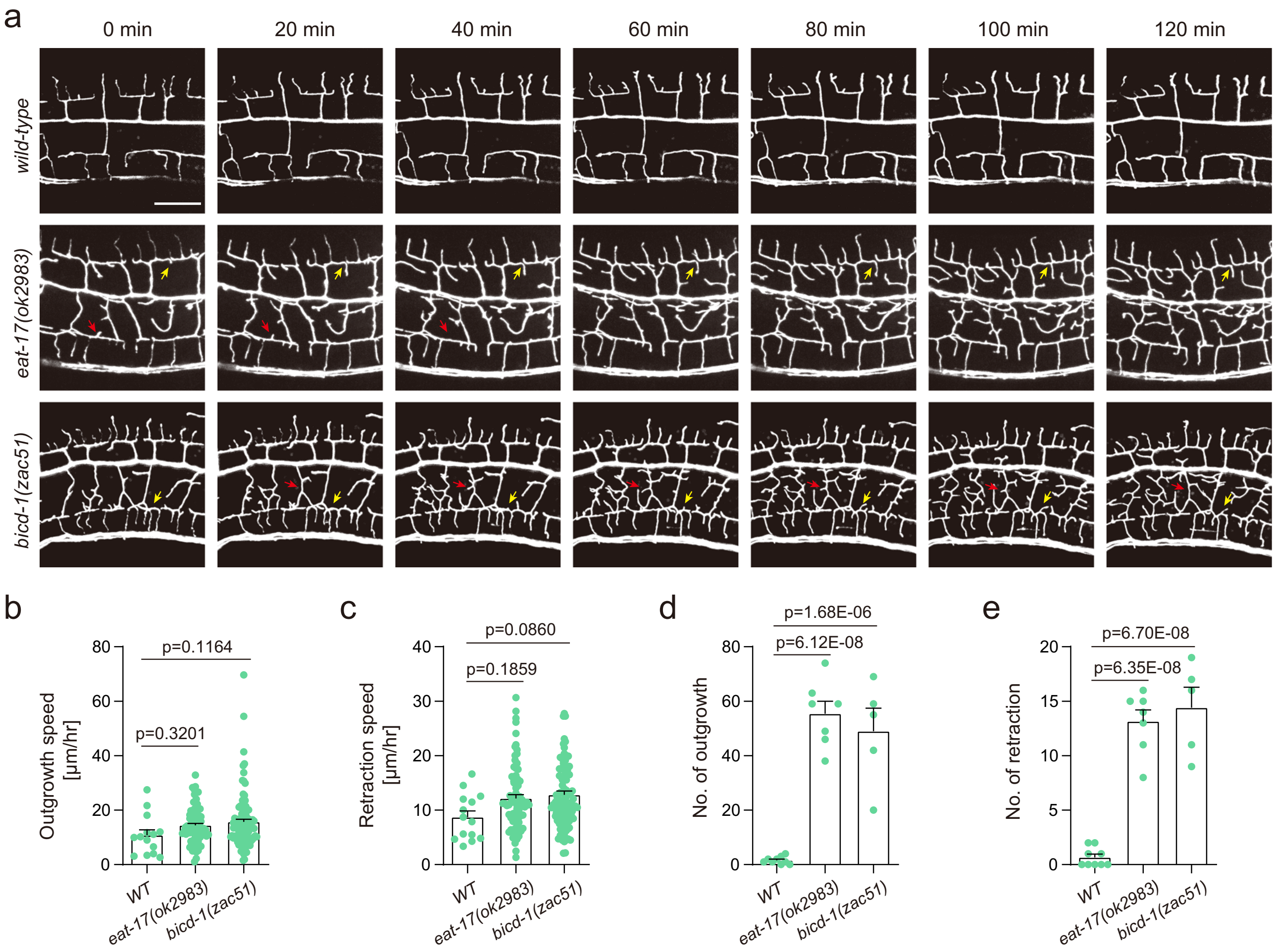

Fig. 2 | Time-lapse analysis of dendrite branching in wildtype, *eat-17* and *bicd-1* mutant animals. a Confocal images from time-lapse videos showing dendrite branch initiation, outgrowth and retraction in wildtype, *eat-17(ok2983)* and *bicd-1(zac51)* mutant animals. Note that both branch initiation-outgrowth (yellow arrows) and retraction (red arrows) were relatively frequently observed in *eat-17* and *bicd-1* mutant animals, but at a very low frequency in the wildtype animals. Scale bar, 20 µm. **b**, **c** The speed of outgrowth (**b**) and retraction (**c**) of ectopic branches during the 2 h period of L4 growth. All values are presented as mean ± s.e.m. ns: not significant (one-sided ANOVA with the Tukey correction). **d**–**e** The number of initiation-growth events (**d**) and retraction (**e**) of ectopic branches during the 2 h period of L4 growth. All values are presented as mean ± s.e.m. ns: not significant. $^{****}p < 0.0001$ (one-sided ANOVA with the Tukey correction). *WT:* $n = 9$ animals; *eat-17 (ok2983):* $n = 7$ animals; *bicd-1(zac51):* $n = 5$ animals. For (**b**–**e**) source data are provided as a Source Data file.

EAT-17 genetically and physically acts together with the dynein adaptor protein BICD-1

To understand the molecular mechanism of EAT-17 in regulating dendrite morphogenesis, we performed a large-scale forward genetic screen to identify mutants that showed similar dendrite formation defects. After screening for ~30,000 haploid genomes, we identified multiple *eat-17*-like mutants. By performing complementation test, we found that *zac26*, *zac45*, *zac54* and *zac106* were new alleles of *eat-17* (Supplementary Fig. 3a-d). Interestingly, all missense mutations were in the CC2 and CC3 coding regions, but not in the RAB GAP coding

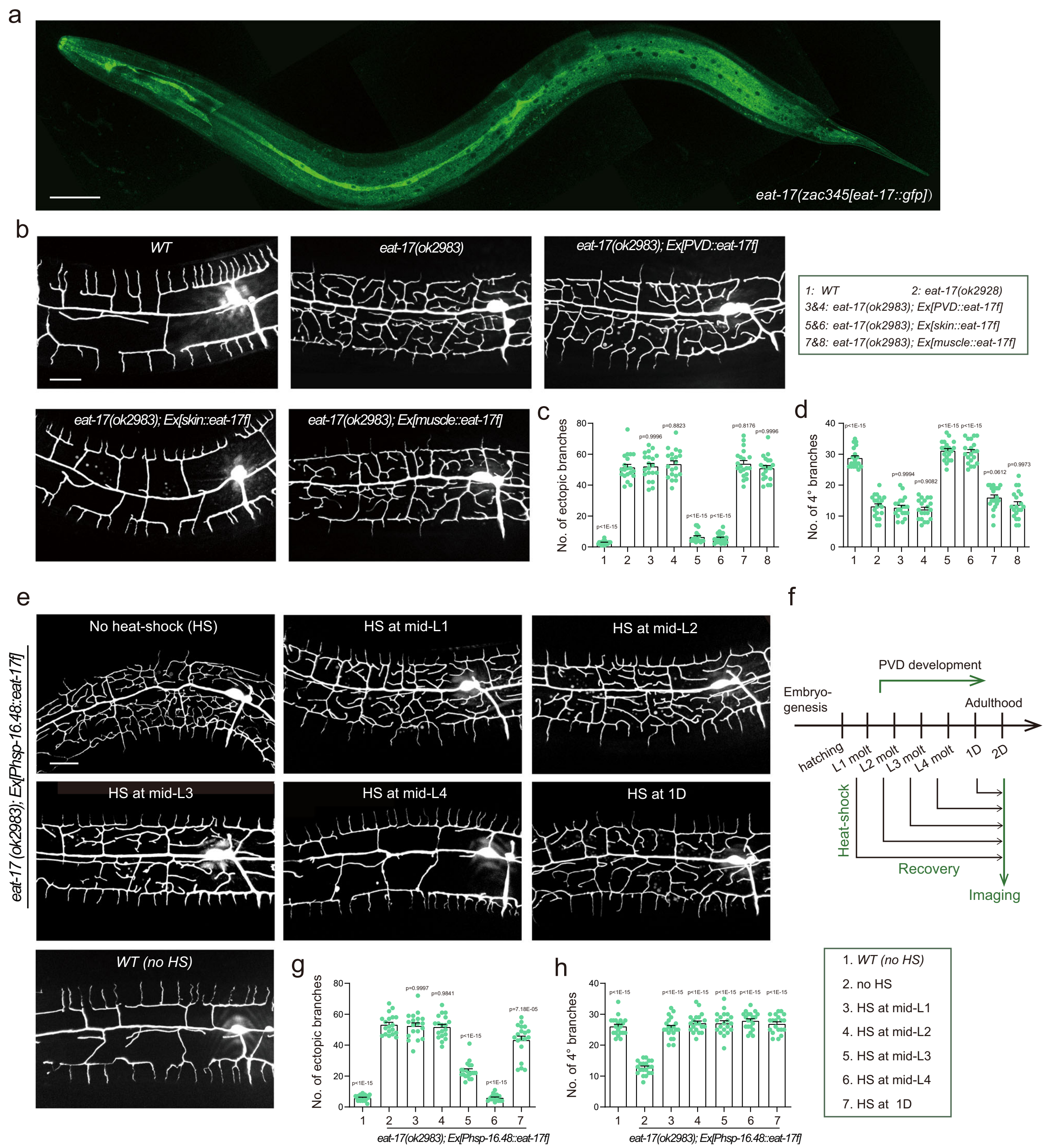

Fig. 3 | EAT-17 functions in the epidermis to regulate dendrite formation. a A confocal image to show the expression pattern of the endogenous EAT-17. The experiment was repeated >3 times with similar results. Scale bar, 50 µm. **b** Confocal images of PVD morphologies of wildtype, *eat-17(ok2983)*, *eat-17 (ok2983)* carrying distinct EAT-17F transgene driven by skin, muscle and PVD-specific promoters, respectively. All animals were at 1 day old adult stage. Scale bar, 20 µm. **c**, **d** Quantification of number of ectopic branches (**c**) and 4° branches (**d**) in a 100 µm region anterior to the PVD cell body for each strain. All values are presented as mean ± s.e.m. ns: not significant. $^{****}p < 0.0001$ (one-sided ANOVA with the Tukey correction). $n = 20$ animals for each column. **e** Confocal images to show the PVD dendrite morphologies of *eat-17(ok2983) Ex[Phsp-16.48::eat-17f]* with different treatments, including no heat-shock control and with heat-shock at distinct developmental stages. All animals were imaged at the 2 day old adult stage (48 h post L4 stage). Scale bar, 20 µm. **f** A cartoon showing the timing of PVD neurogenesis and time points when heat-shock treatment was performed. Note that after heat-shock treatment, animals were cultured at 20 °C to recover until subjected to confocal imaging. **g**, **h** Quantification of number of ectopic branches (**g**) and 4° branches (**h**) in a 100 µm region anterior to the PVD cell body for each strain. All values are presented as mean ± s.e.m. ns: not significant. $^{****}p < 0.0001$ (one-sided ANOVA with the Tukey correction). $n = 20$ animals were quantified for each column. For (**c**–**h**) source data are provided as a Source Data file.

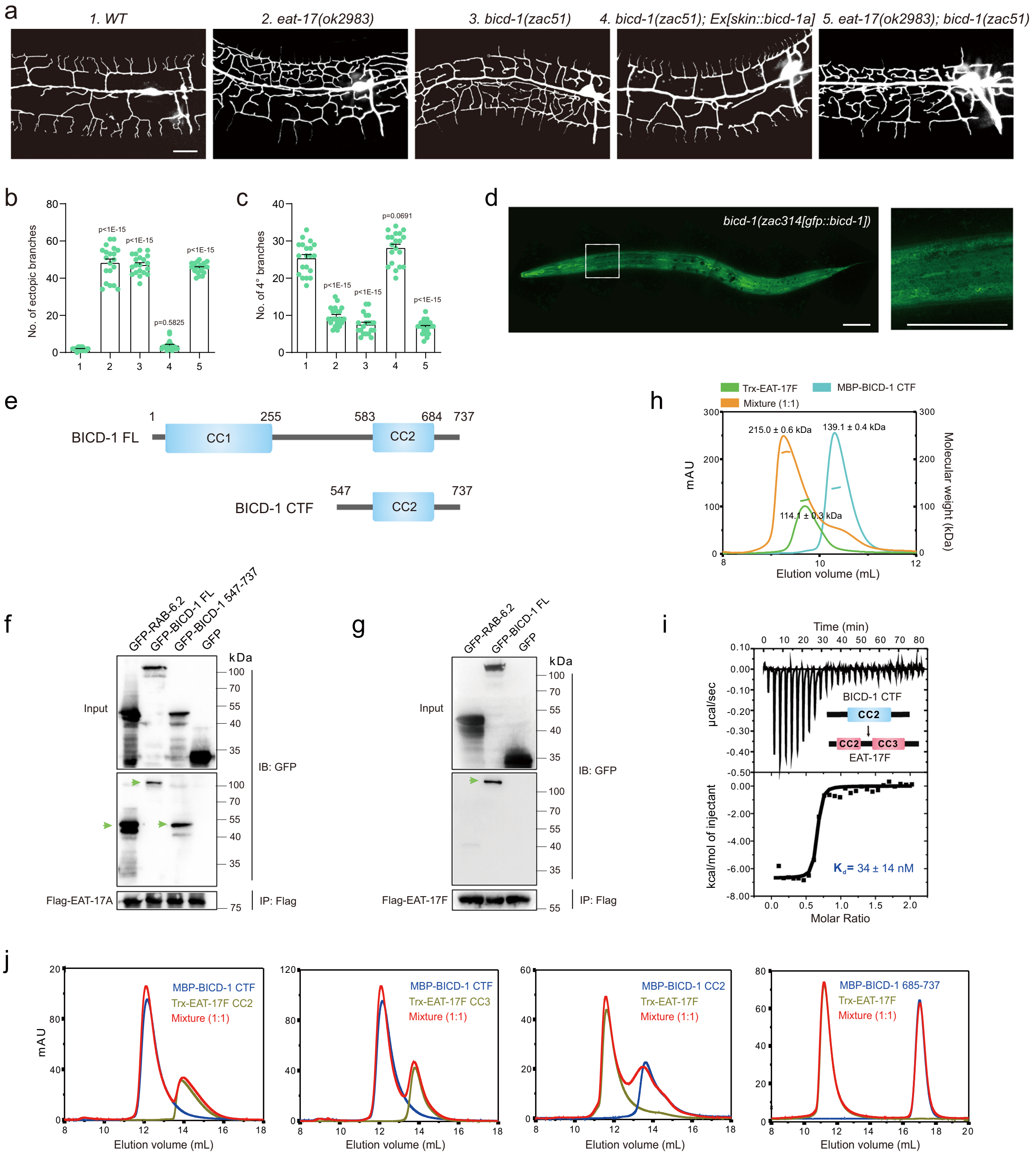

region (Supplementary Fig. 3a). *zac51* phenocopies *eat-17(ok2983)* and the trans-heterozygous progenies showed normal PVD dendrite morphologies, suggesting that *zac51* affects a different gene (Fig. 4a–c). By performing genetic mapping and whole-genome sequencing, we found that *zac51* carried a G-to-A mutation (Q685stop in BICD-1A) in the coding region of *bicd-1*, which encodes a dynein adaptor protein. Knockdown of *bicd-1* generated a similar dendrite morphogenesis defect as that in *bicd-1(zac51)* mutant animals, while a previously reported deletion allele of *bicd-1*, *ok2731*, showed much milder defects. (Supplementary Fig. 4a–f)[33]. A previous study reported that BICD-1 functions in PVD neurons to inhibit ectopic branching[33]. We performed tissue-specific transgene rescue experiments and found that expressing BICD-1 in the epidermis of *bicd-1(zac51)* mutant animals fully rescued the dendrite development defects, while expressing BICD-1 in PVD neurons or body wall muscles failed to do so (Fig. 4a–c, and Supplementary Fig. 4d–f). A functional *gfp::bicd-1* knock-in strain showed that endogenous BICD-1 was expressed in the epidermis and some other tissues (Fig. 4d and Supplementary Fig. 1a–d). *bicd-1(zac51); eat-17(ok2983)* double mutants showed no enhanced ectopic branching defect compared with either of the single mutants, suggesting that these two genes act in the same genetic pathway to inhibit ectopic branching (Fig. 4a–c). The double mutants also showed similar number of 4° branches to either of the single mutants (Fig. 4c). By performing time-lapse recording, we found that *bicd-1(zac51)* animals also showed increased number of branch initiation and retraction events in the lateral region (Fig. 2a–e). A

Fig. 4 | The dynein adaptor protein BICD-1 acts together with EAT-17 to regulate dendrite formation. a Confocal images to show the dendrite PVD morphologies of wildtype, *eat-17(ok2983)*, *bicd-1(zac51)*, *bicd-1(zac51) Ex[skin::bicd-1a]* and *bicd-1(zac51); eat-17(ok2983)*. All animals were at 1 day old stage. Scale bar, 20 μm. **b**, **c** Quantification of number of ectopic branches (**b**) and 4° branches (**c**) in a 100 μm region anterior to the PVD cell body for each strain showed in (**a**). All values are presented as mean ± s.e.m. ns: not significant. ****$p < 0.0001$ (one-sided ANOVA with the Tukey correction). $n = 20$ animals were quantified for each column. **d** Confocal images to show the expression pattern of *gfp::bicd-1* knockin animals. Note that endogenous BICD-1 can be observed in multiple tissues, including the epidermis. The experiment was repeated >3 times with similar results. Scale bar, 100 μm. **e** Schematic diagram to show the domains of BICD-1 full length (FL) and the C-terminal fragment (CTF) of BICD-1. CC: coiled-coil domain. **f**, **g** Results of coimmunoprecipitation assays. The experiment was repeated >3 times with similar results. For (**f**) Flag::EAT-17A was used as the bait protein. Note that GFP tagged-RAB-6.2, BICD-1 FL and BICD-1 CTF could be coimmunoprecipitated. For (**g**) Flag::EAT-17F was used as the bait protein. Note that GFP::BICD-1, but not GFP::RAB-6.2, could be coimmunoprecipitated. IP: immunoprecipitation; IB: immuneblotting. **h** FPLC coupled with static light scattering analysis of Trx-EAT-17F (green line), MBP-BICD-1 CTF (blue line), and the Trx-EAT-17F/ MBP-BICD-1 CTF complex (orange line), showing that both EAT-17F and BICD-1 CTF are dimers in solution and they form a stable complex with molar ration of 2:2. **i** ITC-based measurements of the binding affinity of the BICD-1 CTF with EAT-17F. The K_d error is the fitting error obtained using a 1-site binding kinetics model in Origin 7.0 to fit ITC data. BICD-1 CTF (200 μM) were titrated to EAT-17F (20 μM). The dissociation constant (K_d ~34 nM) indicates a strong binding between BICD-1 and EAT-17F. **j** Analytical gel filtration chromatography (FPLC) analysis showed that neither Trx-EAT-17F CC2 nor CC3 domain only could interact with BICD CTF (the left two panels). Meanwhile, only CC2 domain of BICD-1 CTF or the C-terminal loop (685-737) also lose the interaction abilities with EAT-17F. For (**b**–**j**) source data are provided as a Source Data file.

previous study reported that loss of *dli-1* also causes ectopic branching in the lateral epidermal regions[34]. The ectopic branching phenotype in *dli-1(RNAi); eat-17(ok2983)* double mutants was not more severe than either of the single mutants, indicating that EAT-17, BICD-1, and dynein likely act together to restrict ectopic branching (Supplementary Fig. 5a–c).

Since *eat-17* and *bicd-1* genetically function together, we sought to determine whether they physically interact with each other to form a protein complex. Coimmunoprecipitation assay showed that both long and short isoforms of EAT-17 interacted with GFP-tagged full-length BICD-1, but not the GFP negative control (Fig. 4e–g). A previous study reported that EAT-17 interacted with RAB-6.2[28]. We confirmed that the long isoform, but not the short isoform, indeed interacted with RAB-6.2 (Fig. 4f, g). We also expressed these two proteins in *E. coli* and obtained highly purified proteins. Fast protein liquid chromatography (FPLC) coupled with static light scattering demonstrated that EAT-17F and BICD-1 C-terminal fragment (CTF) form a stable 2:2 complex in solution. The results showed that both EAT-17F and BICD-1 CTF are dimers. When proteins were mixed at a 1:1 molar ratio, the complex peak was formed with a measured molecular weight of ~215.0 kDa, matching well with the molecular weight of a complex comprising 1 copy of EAT-17F dimer and 1 copy of BICD-1 CTF dimer (Fig. 4h). We also performed isothermal titration calorimetry (ITC) analysis and showed that EAT-17F can interact with BICD-1 CTF with high affinity (K_d = ~34 nM) (Fig. 4i). Furthermore, we generated a series of truncated EAT-17F and BICD-1 CTF proteins to map the binding regions on both proteins and found that all the truncations we made abolished the binding (Fig. 4j). Each coiled-coil domain of EAT-17F is necessary for the interaction with BICD-1, and the CTF of BICD-1 is also necessary to retain the interaction. Together, our results suggest that EAT-17 and the dynein adaptor protein BICD-1 act together to regulate PVD dendrite morphogenesis.

EAT-17 and BICD-1 downregulate the dendrite branching ligand SAX-7 in the lateral region of the epidermis

Previous studies showed that PVD dendrite morphogenesis is controlled by an epidermis-localized dendrite branching ligand complex, which contains SAX-7/L1CAM, MNR-1/Menorin and LECT-2/LECT2[11,13–15]. Importantly, SAX-7 is enriched in the dorsal and ventral muscle regions and forms stripes to precisely guide dendrite branch formation[24]. Zhu et al., reported that loss of *dli-1*, which encodes the dynein light intermediate chain, caused ectopic SAX-7 localization and branching in the lateral region[34]. We sought to determine whether the ectopic branching in the *eat-17* and *bicd-1* mutants was also due to ectopic SAX-7 distribution in the lateral epidermis. We examined wildtype, *eat-17* and *bicd-1* mutant animals carrying a transgene *wyIs5000S*, which specifically expresses SAX-7::GFP in the epidermis[24]. Indeed, an ectopic SAX-7::GFP signal was observed in both mutants when compared with the wildtype control animals. Ectopic SAX-7 was distributed in the lateral region, which correlated with the distribution of the ectopic branches (Supplementary Fig. 6a, b). The ectopic SAX-7 distribution could be either a cause or a consequence of ectopic dendrite branching. To distinguish the two possibilities, we further knocked out the *mec-3* gene, loss of which caused a much-simplified dendrite morphology by suppressing both normal and ectopic branch formation[30,35]. Ectopic distribution of SAX-7::GFP in the lateral region was still observed in the *mec-3; eat-17* and *mec-3; bicd-1* mutants (Supplementary Fig. 6a, b). As SAX-7::GFP was overexpressed from the high-copy transgene *wyIs5000S* in this set of experiments, we further generated an endogenous SAX-7::GFP knock-in strain. GFP knock-in did not affect the function of endogenous SAX-7, as PVD dendrite morphogenesis was normal in this strain (Supplementary Fig. 1a–d). In *eat-17(lf)* mutant animals, a similar abnormal accumulation of endogenous SAX-7::GFP was observed in the lateral regions of the epidermis, and their signals were colocalized with the myristoylated-blue fluorescent protein (MYR::BFP) on the epidermal plasma membranes[36]. The ectopic distribution of the endogenous SAX-7::GFP was fully abolished by expressing EAT-17F in the epidermis, and not suppressed by the *mec-3* loss-of-function mutation (Fig. 5a–d). These results suggested that the ectopic accumulation of endogenous SAX-7 on the lateral epidermal plasma membranes of *eat-17* and *bicd-1* mutants was likely the cause of ectopic branching.

PVD neurons form Menorah-like dendrite branches, which rely on the SAX-7-MNR-1-LECT-2-DMA-1 ligand-receptor complex[2,4,5]. To further test the hypothesis that ectopic accumulation of SAX-7 in the *eat-17* and *bicd-1* mutants causes ectopic dendrite branching, we created a double mutant strain, *sax-7; eat-17*, and found that knockout of the dendrite branching ligand *sax-7* not only abolished the normal branching of high-ordered dendrites (3° and 4°) but also suppressed ectopic branching in the lateral epidermal region (Fig. 5e, f). Similar suppression of ectopic branching was observed when we knocked out the other two ligand coding genes *mnr-1* and *lect-2*, and the dendritic receptor coding gene *dma-1* in the *eat-17* mutant background (Fig. 5e, f). Together, our results suggest that the EAT-17-BICD-1 protein complex acts in the epidermis to restrict ectopic dendrite branching via regulating the proper distribution of the dendrite branching ligand SAX-7/L1CAM.

EAT-17 and BICD-1 promote endocytic degradation of the dendrite branching ligand SAX-7

How do EAT-17 and BICD-1 negatively regulate SAX-7 distribution in the lateral region of the epidermis? We speculated that they promoted the endocytosis of SAX-7 on epidermal plasma membranes. If this hypothesis was true, we predicted that: (1) SAX-7 should be detected in the endosomes/ lysosomes in wildtype animals and the endosome/ lysosome distribution should be reduced in *eat-17(lf)* and *bicd-1(lf)*

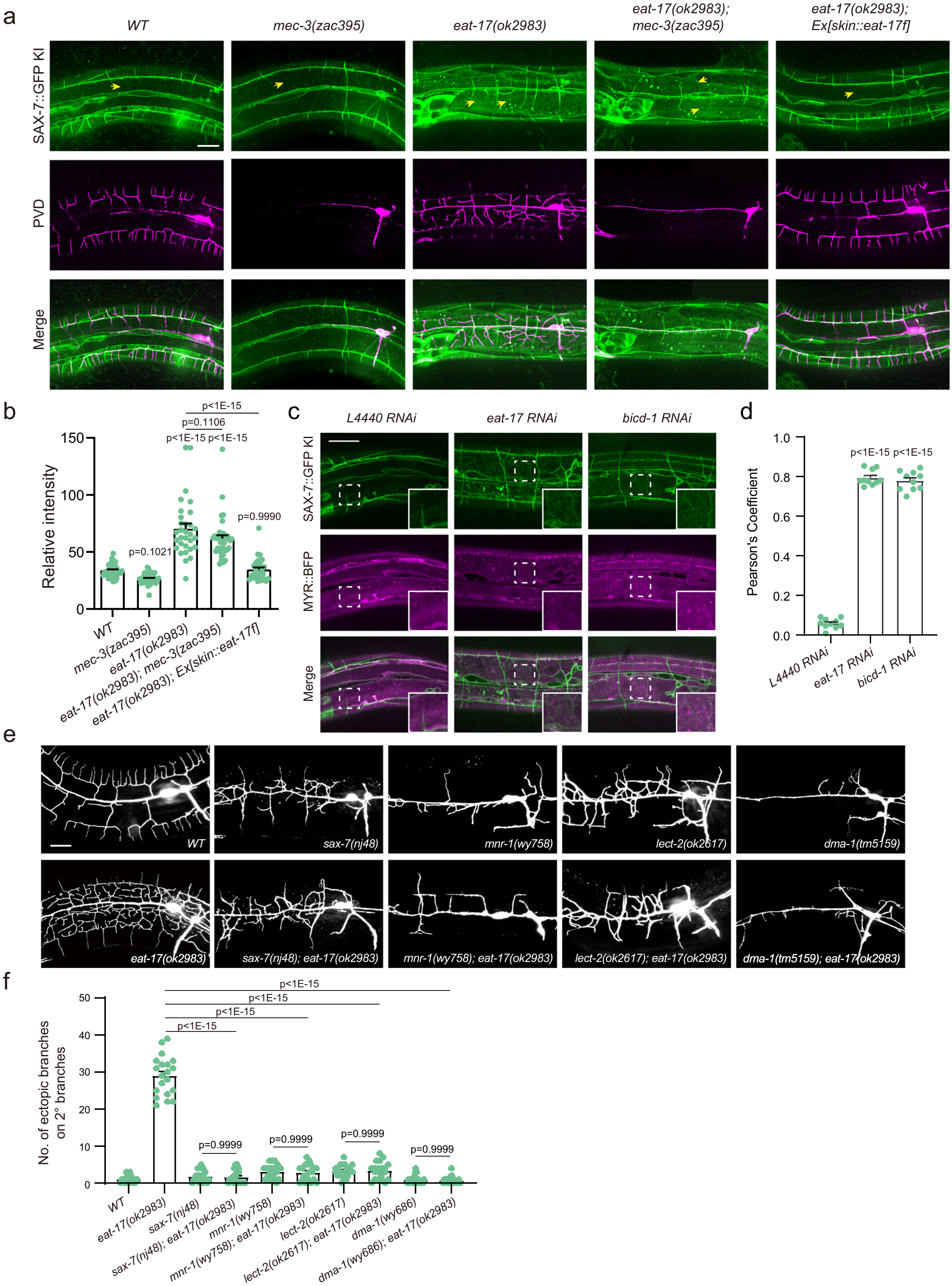

animals; (2) inactivation of endocytosis genes should generate similar ectopic SAX-7 localization and dendrite branching phenotypes. Firstly, we inserted the coding sequence of mCherry into the *sax-7* endogenous locus to generate SAX-7::mCherry. Unlike GFP, mCherry is not sensitive to the acidic environment (such as the lumen of the endosomes and lysosomes)[37]. Similar to endogenous SAX-7::GFP localization, the endogenous SAX-7::mCherry was enriched at the sublateral tertiary lines, guiding the formation of PVD tertiary dendrites[11,13]. In addition, punctate signals were also observed, likely representing SAX-7::mCherry within endocytic compartments. Indeed, a subset of SAX-7::mCherry-positive puncta was co-labeled with several markers of early endosomes, including GFP::RAB-5[38], YFP::2xFYVE[39] and RME-8::GFP[40,41]. Moreover, the majority of the SAX-7-positive puncta were found within the late endosomes and lysosomes, as indicated by their

Fig. 5 | Loss of *eat-17* and *bicd-1* cause ectopic accumulation of the dendrite branching ligand SAX-7 in the lateral region of the epidermis. a Confocal images showing the distribution of the endogenous SAX-7::GFP and PVD dendrite morphologies in different strains. Arrows: lateral epidermal regions. Scale bar, 20 μm. **b** Quantifications of the fluorescence intensity of the endogenous SAX-7::GFP in the lateral region in different strains showed in (**a**). All values are presented as mean ± s.e.m. *WT:* $n = 41$ animals; *mec-3(zac395):* $n = 34$ animals; *eat-17(ok2983):* $n = 31$ animals; *eat-17(ok2983);mec-3(zac395):* $n = 37$ animals; *eat-17(ok2983) Ex[skin::eat-17f]:* $n = 28$ animals. ns: not significant. ****$p < 0.0001$ (one-sided ANOVA with the Tukey correction). **c** Confocal images showing the distribution of the endogenous SAX-GFP and exogenous MYR::BFP (as a marker for the epidermal plasma membranes). The image in the lower right corner was 2 times enlarged. Scale bar, 20 μm. **d** Co-localization analysis for the endogenous SAX-7::GFP and the epidermal plasma membrane marker (MYR::BFP) in different strains. All values are presented as mean ± s.e.m. ns: not significant. ****$p < 0.0001$ (one-sided ANOVA with the Tukey correction). $n = 10$ animals were imaged and quantified for each column. **e** Confocal images showing the PVD dendrite morphologies of wildtype, *eat-17(ok2983)*, *sax-7(nj48)*, *sax-7(nj48); eat-17(ok2983)*, *mnr-1(wy758)*, *mnr-1(wy758); eat-17(ok2983)*, *lect-2(ok2617)*, *lect-2(ok2617); eat-17 (ok2983)*, *dma-1 (tm5159)* and *dma-1(tm5159); eat-17(ok2983)*. All animals were at 1 day old stage. Scale bar, 20 μm. **f** Quantification of number of ectopic 3° branches derived from 2° branches in a 100 μm region anterior to the PVD cell body in the strains showed in (**e**). All values are presented as mean ± s.e.m. ns: not significant. ****$p < 0.0001$ (one-sided ANOVA with the Tukey correction). $n = 20$ animals were quantified for each column. For (**b**–**f**) source data are provided as a Source Data file.

co-localization with GFP::RAB-7[38] and SCAV-3::GFP[42] (Fig. 6a, b). Notably, overexpression of a constitutively active form of RAB-5 (RAB-5 Q78L) in the epidermis disrupted endosome maturation, resulting in abnormally enlarged endosomes, the majority of which contained SAX-7::mCherry. Knockdown of *eat-17* and *bicd-1* dramatically reduced the presence of SAX-7 in these enlarged endosomal compartments, suggesting that SAX-7 is endocytosed in an EAT-17- and BICD-1-dependent manner (Fig. 6c, d, and Supplementary Fig. 7a, b).

To more sensitively compare the endocytosis rate of SAX-7 in wild type, *eat-17(lf)* and *bicd-1(lf)* animals, we combined the Cre-LoxP and heat shock-induced transgene expression systems. This strategy allowed us to selectively and temporarily induce a batch of SAX-7::mCherry proteins in the epidermis and perform a time-course assay (Supplementary Fig. 8a, b)[43]. In all three strains, a similar amount of SAX-7 was observed around the sublateral tertiary lines, suggesting that SAX-7 expression and secretion were unaffected by *eat-17* or *bicd-1* knockdown (Supplementary Fig. 8c, d). In wild type animals, SAX-7::mCherry proteins were observed in RME-8-labeled early endosomes and SCAV-3-labeled lysosomes as early as 3 h after heat shock. The intensity of SAX-7 gradually increased at later time points, likely because more SAX-7 proteins were endocytosed. Strikingly, knockdown of *eat-17* or *bicd-1* reduced the amount of SAX-7 in the endo-lysosomal compartments at various time points following heat shock (Supplementary Fig. 9a–f). Together, these results suggest that EAT-17 and BICD-1 play critical roles in facilitating the efficient endocytosis-dependent downregulation of SAX-7 in the epidermis.

Next, we inactivated four conserved genes regulating endo-lysosomal trafficking, including *rab-5/RAB5*, *dyn-1/DNM1*, *dpy-23/AP2M1* and *chc-1/CLTC*[44]. As these genes are essential for development, we performed epidermis-specific conditional knockout using either a ribozyme-based Ribo-Off method developed by ourselves recently or a modified version of somatic CRISPR (Supplementary Fig. 10a, b)[45,46]. Knockout of all four genes in the epidermis indeed generated *eat-17*-like ectopic branching in the lateral epidermal region (Supplementary Fig. 10c, d). Alternatively, we performed RNA interference experiments by feeding gene-specific double-stranded RNAs to wildtype animals at the L2 stage and examining the dendrite branching phenotype at the 1 day old adult stage (24 h post the L4 stage). Knockdown of the endocytosis genes *rab-5* and *dyn-1* generated not only ectopic accumulation of SAX-7 in the lateral epidermal region but also ectopic branching in the same region (Fig. 7a–d). Our western blotting analysis revealed that loss of *eat-17* and *bicd-1*, as well as the knockdown of *rab-5*, consistently resulted in increased levels of SAX-7 in the epidermis (Supplementary Fig. 11a, b). These findings indicate that EAT-17, BICD-1 and RAB-5 are required for the endocytosis-dependent downregulation of SAX-7. Notably, loss of *eat-17* or *bicd-1* did not further enhance the ectopic branching or ectopic SAX-7 distribution of animals subjected to *rab-5 and dyn-1* knockdown, supporting that they act in the same genetic pathway (Fig. 6a–d).

To gain more insights on how EAT-17 and BICD-1 function to regulate endocytic trafficking, we examined the number of RAB-5-labeled early endosomes in wildtype, *eat-17* and *bicd-1* mutant animals. Both *eat-17(ok2983)* and *bicd-1(zac51)* caused a dramatically reduced number of RAB-5-positive early endosomes, suggesting that EAT-17 and BICD-1 are required for endosome biogenesis (Fig. 6e, f). We also analyzed 2xFYVE and RME-8, two additional endosomal markers[39,41], and found that loss of *eat-17* also resulted in significantly reduced numbers of endosomes labeled by these two reporters (Supplementary Fig. 12a–c). Knock-down the endocytosis genes *chc-1*, *dyn-1* or *dpy-23* generated a similar reduced endosome biogenesis phenotype, and the defects were not further enhanced by loss of *eat-17* or *bicd-1* (Fig. 7e, f). Thus, we concluded that EAT-17 and BICD-1 act together with RAB-5 and other endocytosis regulators to promote endosome biogenesis in *C. elegans* epidermis.

eat-17 mutant animals show defects in locomotion

Previous studies showed that abnormal PVD dendrite morphogenesis affected the proprioceptive function of the PVD neuron, which could be indicated by the amplitude and wavelength of the sinusoidal movements[47]. We sought to determine whether this function was perturbed by the loss of *eat-17*. We used the *dma-1* mutant strain as our positive control, as loss of *dma-1* was reported to result in severe defects in both dendrite branching and proprioception[12,47]. Interestingly, although loss of *eat-17* generated ectopic branching, it severely reduced the amplitude and wavelength of body movements similar to those of the reduced branching *dma-1* mutant animals. Epidermis-specific expression of EAT-17F fully rescued the locomotion defects of the *eat-17(ok2983)* mutants. We measured the body length of wildtype, *dma-1*, *eat-17* and *eat-17* carrying the transgene to express EAT-17F in the epidermis, and found that there was no significant difference, which ruled out the possibility that the difference in amplitude and wavelength was due to differences in body lengths (Fig. 8a–d). In conclusion, EAT-17-dependent proper dendrite morphogenesis is critical for the proprioceptive function of PVD sensory neurons.

Discussion

In this study, we used the *C. elegans* PVD sensory neuron as a model to investigate the mechanism that restricts dendrite branching and found that a previously uncharacterized short isoform of the EAT-17 protein acts together with the dynein adaptor protein BICD-1 and the motor protein dynein to remove the ectopically localized dendrite branching ligand SAX-7 in the lateral region of the epidermis. EAT-17 and BICD-1 act together with the endocytic machinery to downregulate SAX-7 so that ectopic branching does not occur in the wildtype animals (Fig. 8e).

Sasidharan et al., reported that EAT-17 (also known as TBC-4 previously) functioned as the GAP of the small GTPase RAB-10 to promote neuropeptide release from the dense-core vesicles in *C. elegans* motor neurons[25]. EAT-17 and RAB-10 colocalized with each other

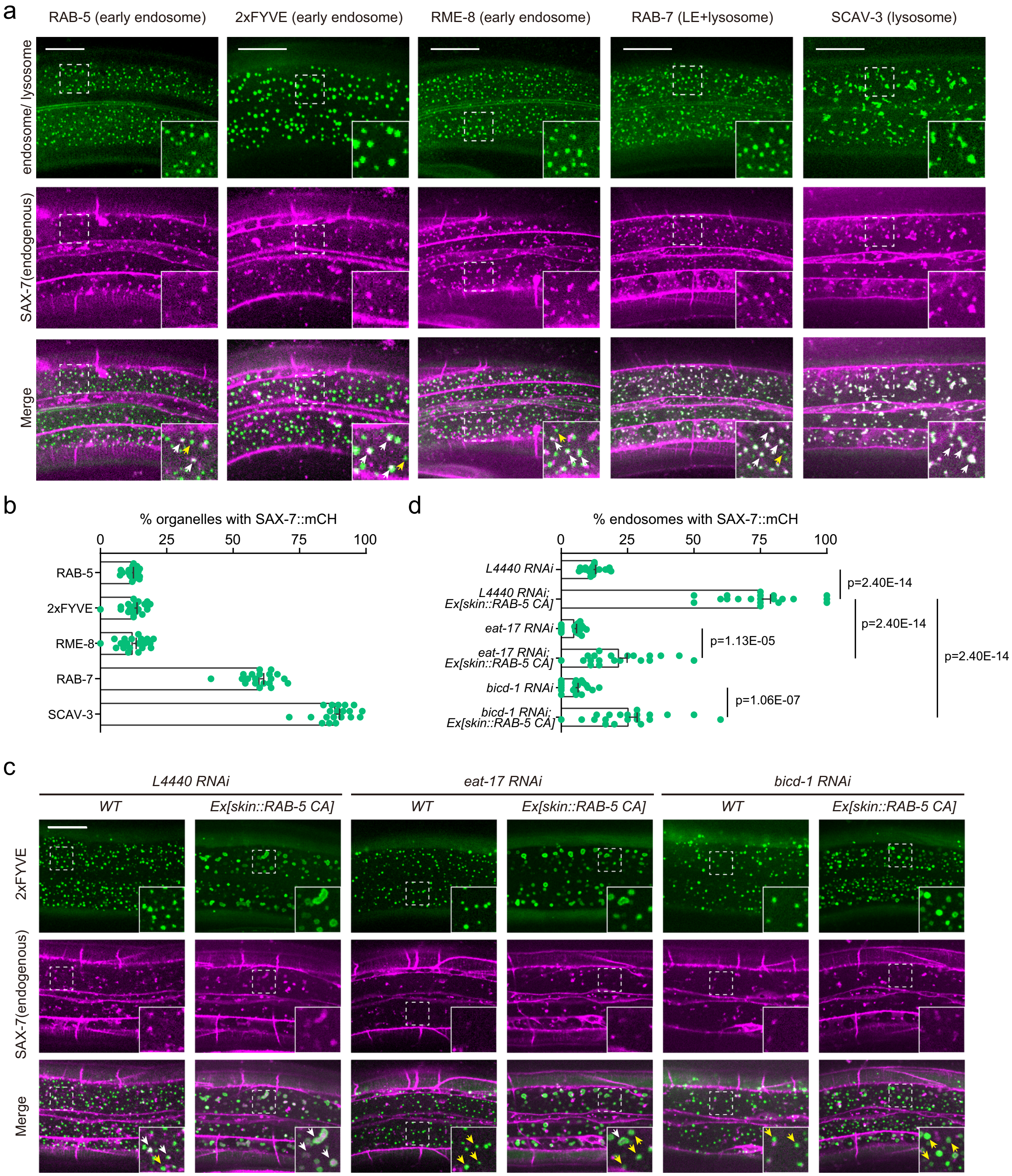

Fig. 6 | Efficient SAX-7 endocytosis in the epidermis relies on both EAT-17 and BICD-1. a Confocal images showing the distribution of endogenous SAX-7::mCherry in early endosomes (labeled by GFP::RAB-5, YFP::2xFYVE or RME-8::GFP), late endosomes (LE) and lysosomes (labeled by GFP::RAB-7) and lysosomes (labeled by SCAV-3::GFP) in epidermal cells in the wildtype. White arrows: organelles positive for SAX-7::mCherry; Yellow arrows: organelles negative for SAX-7::mCherry. The image in the lower right corner was 2 times enlarged. Scale bar, 20 µm. **b** Quantification of the percentage of vesicles with SAX-7::mCherry in their lumen in wildtype animals. All values are presented as mean ± s.e.m. $n = 20$ animals were quantified for each column. **c** Confocal images showing the distribution of endogenous SAX-7::mCherry in endosomal compartments (labeled by YFP::2x-FYVE) in epidermal cells in different strains. RAB-5 CA: constitutively active RAB-5. The image in the lower right corner was 2 times enlarged. Scale bar, 20 µm. **d** Quantification of the percentage of endosomes with SAX-7::mCherry in their lumen for each strain. All values are presented as mean ± s.e.m. ns: not significant. $^{****}p < 0.0001$ (one-sided ANOVA with the Tukey correction). $n = 20$ animals were quantified for each column. For (**b**–**d**) source data are provided as a Source Data file.

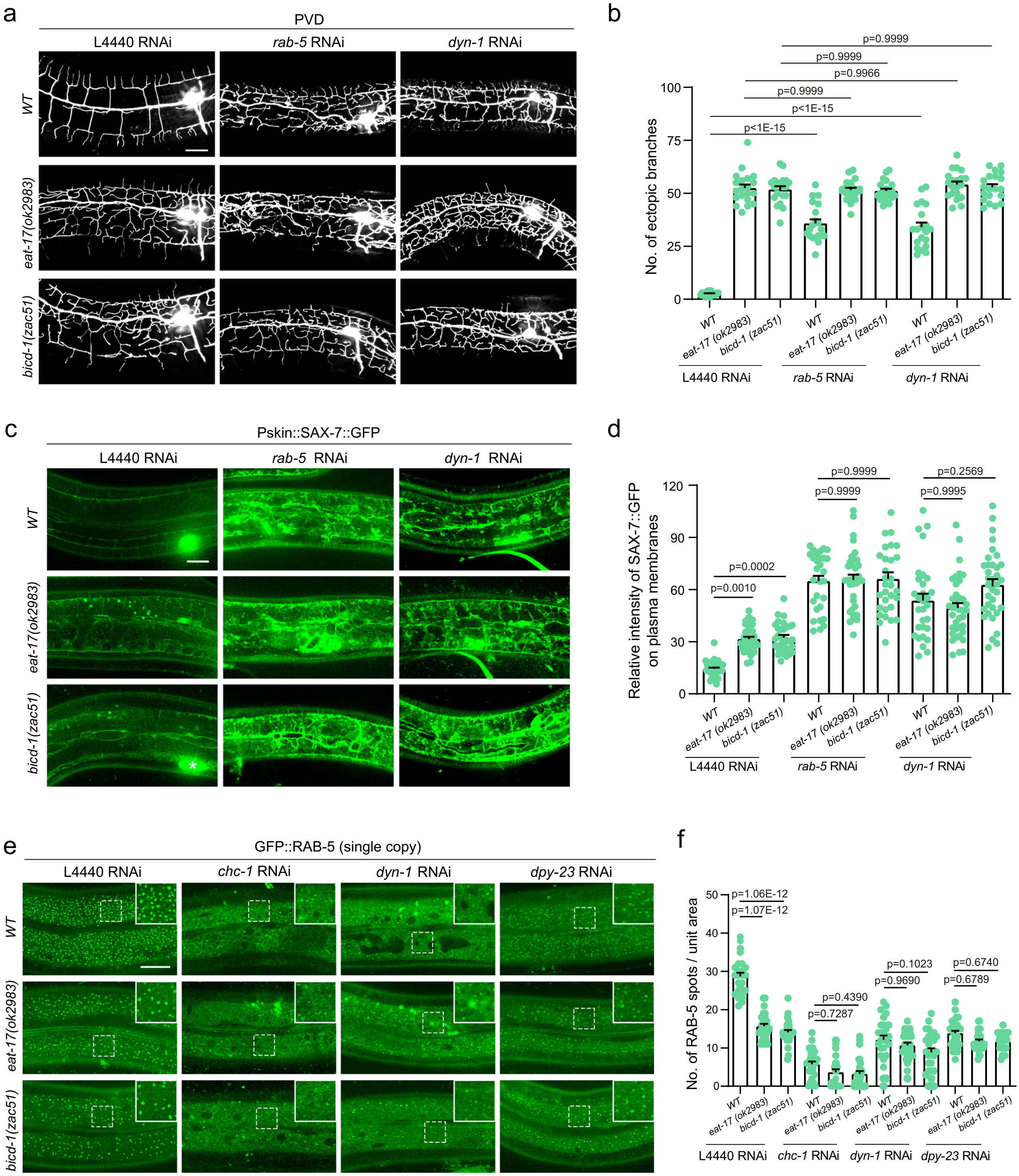

in neuronal cell bodies, and showed interaction in a yeast two-hybrid assay. The neuropeptide secretion defect could be rescued by the wildtype TBC-4 but not a mutant form (EAT-17 R155A) in which the GAP activity is abolished, demonstrating that the long isoform acts as the GAP of RAB-10. In another study, Straud et al., found that EAT-17 interacted with RAB-6.2, and they were co-expressed in the terminal bub muscle to promote grinder formation, possibly by facilitating secretion of proteins which are components of the grinder[28]. In these two cases, EAT-17 long isoforms function as a GAP to enhance the GTPase activity of RAB-10 or RAB-6.2. Here, we found that a previously uncharacterized short isoform(s) is sufficient to regulate proper PVD dendrite morphogenesis. Several lines of evidences support this notation. First, knockdown all the isoforms showed dendrite morphogenesis defects, while knockdown the long isoforms showed normal morphology. Second, dendrite development was not perturbed by the mutations affecting the long isoforms which encode EAT-17 proteins with a RAB GAP domain. Last, expressing either a short isoform (EAT-17F) or a long isoform (EAT17A or EAT-17D) was sufficient to restore normal PVD dendrite morphology. Our results support that besides the previously reported exocytosis functions, EAT-17 can also act in the endocytic degradation pathway, which is critical for proper dendrite morphogenesis.

Fig. 7 | EAT-17 and BICD-1 function in the endocytosis pathway to downregulate the branching ligand SAX-7. a Confocal images to show PVD dendrites in wildtype, *eat-17(ok2983)* and *bicd-1(zac51)* treated with either control (empty vector) RNAi, *rab-5* RNAi, or *dyn-1* RNAi, respectively. An integrated transgene *wyIs592 [ser2-prom3::myri-gfp]* was used to label PVD dendrites. Scale bar, 20 µm. **b** Quantification of number of ectopic branches in the lateral regions of different strains showed in (**a**). All values are presented as mean ± s.e.m. ns: not significant (one-sided ANOVA with the Tukey correction). $n = 20$ animals were quantified for each column. **c** Confocal images to show SAX-7::GFP in wildtype, *eat-17(ok2983)* and *bicd-1(zac51)* treated with either control (empty vector) RNAi, *rab-5* RNAi, or *dyn-1* RNAi, respectively. *wyIs50005 [Pdpy-7::sax-7::gfp + ser2prom3::myri-mcherry]* was used to label SAX-7 in the epidermis. Asterisks: ectopic GFP expression in the spermatheca. Scale bar, 20 µm. **d** Quantifications of the relative fluorescence intensity of SAX-7::GFP in the lateral region in different strains showed in (**c**). All values are presented as mean ± s.e.m. *WT L4440 RNAi:* $n = 33$ animals; *eat-17(ok2983) L4440 RNAi:* $n = 30$ animals; *bicd-1(zac51) L4440 RNAi:* $n = 31$ animals; *WT rab-5 RNAi:* $n = 28$ animals; *eat-17(ok2983) rab-5 RNAi:* $n = 32$ animals; *bicd-1(zac51) rab-5 RNAi:* $n = 30$ animals; *WT dyn-1 RNAi:* $n = 29$ animals; *eat-17(ok2983) dyn-1 RNAi:* $n = 37$ animals; *bicd-1(zac51) dyn-1 RNAi:* $n = 34$ animals. ns: not significant. $^{**}p < 0.01$ (one-sided ANOVA with the Tukey correction). $n \geq 25$ animals were imaged and quantified for each column. **e** Confocal images of GFP::RAB-5 positive spots in the epidermis of different strains, including wildtype, *eat-17(ok2983)* and *bicd-1(zac51)* treated with control RNAi, *chc-1* RNAi, *dyn-1* RNAi, or *dpy-23* RNAi respectively. **f** Quantification of number of GFP::RAB-5 positive vesicles in the strains showed in (**e**). All values are presented as mean ± s.e.m. *WT L4440 RNAi:* $n = 25$ animals; *eat-17(ok2983) L4440 RNAi:* $n = 27$ animals; *bicd-1(zac51) L4440 RNAi:* $n = 27$ animals; *WT chc-1 RNAi:* $n = 27$ animals; *eat-17(ok2983) chc-1 RNAi:* $n = 27$ animals; *bicd-1(zac51) chc-1 RNAi:* $n = 27$ animals; *WT dyn-1 RNAi:* $n = 27$ animals; *eat-17(ok2983) dyn-1 RNAi:* $n = 27$ animals; *bicd-1(zac51) dyn-1 RNAi:* $n = 27$ animals; *WT dpy-23 RNAi:* $n = 29$ animals; *eat-17(ok2983) dpy-23 RNAi:* $n = 27$ animals; *bicd-1(zac51) dpy-23 RNAi:* $n = 27$ animals. ns: not significant. $^{****}p < 0.0001$ (one-sided ANOVA with the Tukey correction). For (**b**–**f**) source data are provided as a Source Data file.

In the epidermis of wildtype animals, SAX-7 forms stripes to guide the formation of tertiary and quaternary branches, which are sandwiched by the epidermis and body wall muscles. It also localizes onto the epidermal-seam cell junctions[23,24]. However, PVD dendrites can ignore the branching signal here as a Furin-like protein KPC-1 acts in the PVD neuron to downregulate the dendrite receptor DMA-1 level on the surface of the dendritic growth cones, possibly via promoting DMA-1 endocytosis or sorting to deliver it into the lysosomes for degradation[23]. In previous studies, ectopically expressed SAX-7 in seam cells, touch receptor neurons or motor neurons are sufficient to guide dendrite branching and growth[11]. Consistent with the previous findings, here we found that in *eat-17* and *bicd-1* mutant animals, ectopically localized SAX-7 in the lateral region of the epidermis was also sufficient to guide the dendrite branching decision within this region. By performing double mutant analysis, we showed that dendrite innervation onto the lateral epidermis not only relied on SAX-7, but also the other dendrite branching ligands (MNR-1 and LECT-2) and the dendrite receptor DMA-1.

The endocytosis machinery plays critical roles during dendrite development. Loss of *RAB5* in *Drosophila* class IV dendrite arborization (DA) neurons causes reduced branching[48]. This clearly shows the pivotal role of the endosomal pathway in dendrite branching and growth, possibly via modulating internalization and subsequent sorting of the dendritic receptors. Consistent with this notion, Yang et al., found that localized clathrin-mediated endocytosis of the cell adhesion molecule L1-CAM promotes the extension of higher-order branches in the *Drosophila* class IV DA neurons[49]. Interestingly, endocytosis-dependent downregulation of L1-CAM is also critical to trigger dendritic thinning and pruning, a process to eliminate unwanted dendritic branches[50,51]. In this study, we find that the endocytosis machinery acts in the non-neuronal epidermal cells to downregulate the surface localization of the dendrite branching ligand SAX-7 to restrict branching in the lateral regions. Thus, the endocytosis pathway can act in both neuronal and non-neuronal cells to regulate dendrite branching, outgrowth, stabilization and pruning.

In two previous studies, *C. elegans* EAT-17 acts as a GAP of RAB-10 to promote neuropeptide release from the motor neurons, or a GAP of RAB-6.2 to promote grinder formation[25,28]. In addition, EVI5 (the homolog of EAT-17 in humans) and Evi5 (the homolog of EAT-17 in *Drosophila*) were reported to act as a GAP of Rab11[52,53]. However, another study showed EVI5 showed no GAP activity for RAB11 in vitro[54]. Here, we find that a previously uncharacterized short isoform of EAT-17 (EAT-17S), which lacks the RAB GAP domain, is sufficient to restrict ectopic branching. EAT-17S functions together with the dynein adaptor protein and the motor dynein to downregulate the localization of the branching ligand SAX-7 on the epidermal cell membranes. Double mutant analysis supports that EAT-17S, BICD-1 and dynein act in the endocytosis pathway. How does EAT-17S act to promote endocytosis? One possibility is that EAT-17S functions as an adaptor protein to link the endosomes with the BICD-1-dynein complex. Future investigation is needed to identify which endosomal protein(s) interacts with EAT-17S. Another possibility is that EAT-17S may function together with BICD-1 to activate the dynein motor. Purified mammalian dynein rarely displays processive motility, suggesting that it is autoinhibited and required activation. Formation of the dynein-dynactin-cargo adaptor complex causes dynein activation. One of the tested cargo adaptors is BICD1[55]. The mammalian BICD1/BICD2 uses its N-terminal part to interact with dynein and dynactin, and its C-terminal part to bind with RAB6[56–59]. The C-terminal part has another function: it binds with the N-terminal part of BICD1 to attenuate its interaction with dynein and dynactin[60]. Thus, it is plausible that BICD-1 (the *C. elegans* homolog of BICD1) plays a similar and conserved role in regulating dynein activation and EAT-17 promotes dynein activation by binding to the C-terminal portion of BICD-1. This will be an interesting direction for future investigation.

Methods

C. elegans genetics

N2 was used as the wildtype strain and all *C. elegans* strains were cultured under standard conditions at 20 °C[61]. The mutant alleles used in this study were *eat-17(ok2983)*, *eat-17(ok2928)*[25], *eat-17(ok3041)*, *eat-17(zac305)*, *eat-17(zac276)*, *eat-17(zac26)*, *eat-17(zac45)*, *eat-17(zac54)*, *eat-17(zac106)*, *bicd-1(ok2731)*[33], *bicd-1(zac51)*, *sax-7(nj48)*[11], *mnr-1(wy758)*[11], *lect-2(ok2617)*[14,15], *dma-1(tm5159)*[15,19], *mec-3(e1338)*[30], *mec-3(zac395)* and *mec-3(zac459)*. Standard microinjection methods were used to generate transgenic lines and genome edited strains (see below). The strains used in this study were listed in the Supplementary Table 1.

Isolation, mapping and cloning of *eat-17* and *bicd-1* mutants

wyIs594 (*ser2prom3::myr-gfp*) animals at the fourth larval stage were treated with 50 mM ethyl methanesulfonate (EMS). Every five F1 animals were transferred onto each plate, and around 100 F2 animals from each plate were examined for abnormal dendrite morphogenesis defects under a fluorescence compound microscope. Animals with such defects were rescued and their progenies were re-examined to see whether the defective phenotypes were stable. *zac26*, *zac45*, *zac54*, and *zac106* were new *eat-17* alleles as they failed to complement *eat-17(ok2983)* allele. *eat-17* genomic DNA was amplified by PCR and sequenced to identify the causal mutations. For *zac51* allele, SNP-SNIP mapping and whole-genome sequencing were used to identify the causal mutation[62,63].

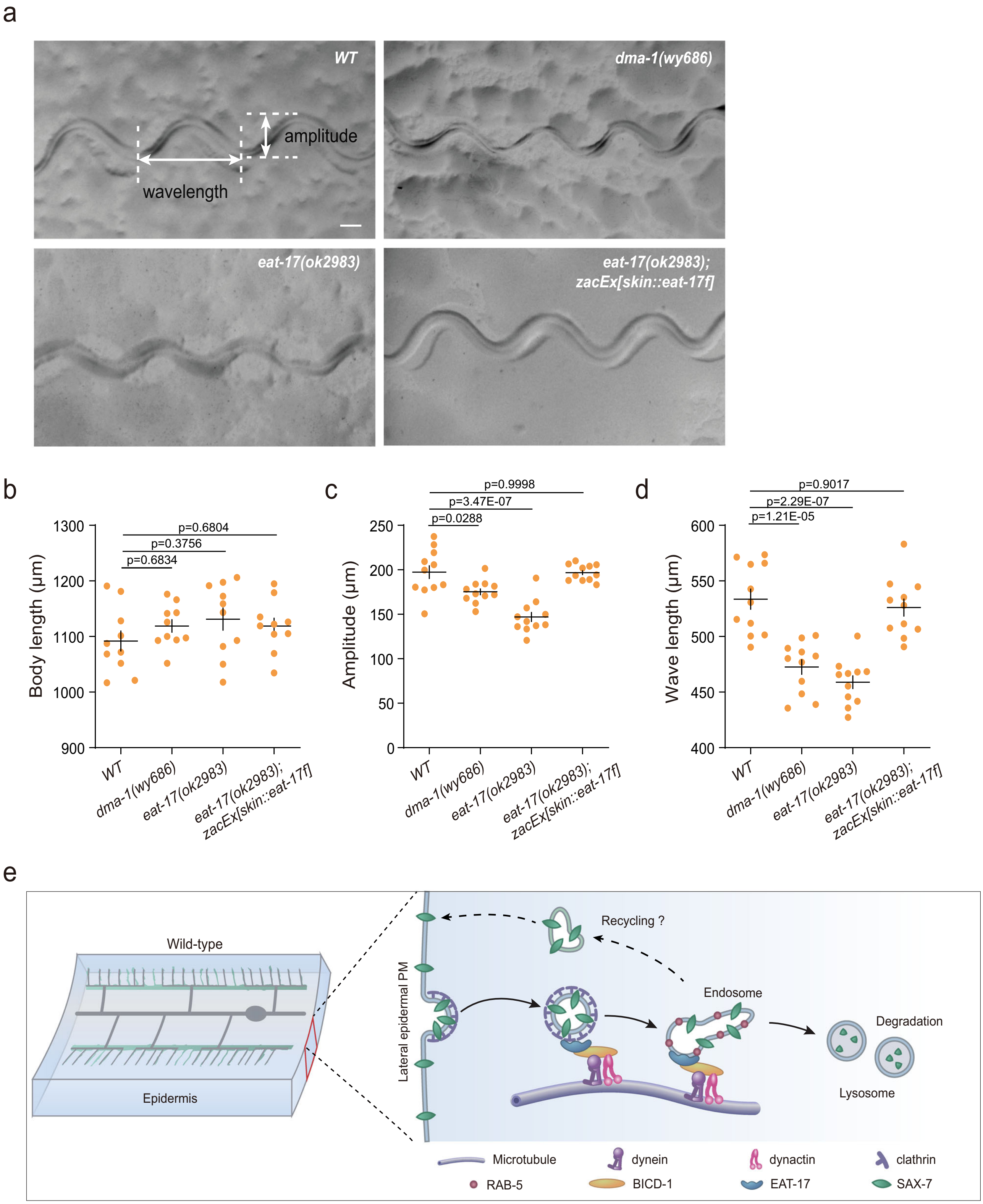

Fig. 8 | Loss of *eat-17* likely affects the proprioceptive function of the PVD neurons. a Representative images to show the moving tracks of wildtype, *dma-1(wy686)*, *eat-17(ok2983)* and *eat-17(ok2983) Ex[skin::eat-17f]* at 1 day old adult stage. Scale bar, 100 μm. **b** Quantification of the body length for the strains showed in (**a**). $n = 10$ animals were quantified for each genotype. All values are presented as mean ± s.e.m. ns: not significant (one-sided ANOVA with the Tukey correction). **c**, **d** Quantification of amplitude (**c**) and wavelength (**d**) of the moving tracks for the genotypes indicated ($n = 11$ animals for each genotype). All values are presented as mean ± s.e.m. ns: not significant, $^*p < 0.05$, $^{****}p < 0.0001$ (one-sided ANOVA with the Tukey correction). **e** A cartoon to show that EAT-17 acts together with BICD-1, the dynein complex and other endocytosis regulators to promote SAX-7 endocytosis from the lateral plasma membranes. The endocytosed SAX-7 is delivered into the lysosomal degradation pathway or potentially recycled back to the plasma membranes. For (**b**–**d**) source data are provided as a Source Data file.

CRISPR/Cas9-mediated genome editing

To generate *eat-17(zac345[eat-17::gfp])*, a donor plasmid (5’ homology arm+ *gfp* + 3’ homology arm) with silent mutations (50 ng/μL), *eft-3p::cas9* (50 ng/μL, kindly provided by Dr. Suhong Xu) and two plasmids to express single-guide RNAs (sgRNA#1: 5’TTGACAAAGCGTCGTCTAG3’, sgRNA#2: 5’GGATTCGGGTGTACAACTGT3’, 25 ng/μL each), and negative selection markers *odr-1p::rfp* (30 ng/μL), *myo-2p::mcherry* (Addgene #19327; 2 ng/μL), and *myo-3p::mcherry* (Addgene #19328; 3 ng/μL) were mixed and injected into *unc-119(ed4)*. Noted that *gfp* coding sequence in the repair donor plasmid was amplified from pMLS252 (Addgene #73720) and contained *Cbr-unc-119(+)* in one of the introns[64]. After a week, progenies that did not express any of the negative selection markers and moved normally were selected for PCR-based genotyping and Sanger sequencing. No additional mutation was found based on the Sanger sequencing results. A similar protocol was used to generate *sax-7(zac311[sax-7::gfp]), sax-7(zac421[sax-7::mCherry])* and *bicd-1(zac314[gfp::bicd-1])*. sgRNA#1: 5’GTCGACGTTGATCCTTTCT3’ and sgRNA#2: 5’TCGACGTTGATCCTTTCTC3’ were used to generate *sax-7(zac311[sax-7::gfp])* and *sax-7(zac421[sax-7::mCherry])*. sgRNA#1: 5’ACAATGGCTGAATCAGAAT3’ and sgRNA#2: 5’TAAATTTCAGCAGCCACAA3’ were used to generate *bicd-1(zac314[gfp::bicd-1])*.

A similar protocol was used to generate the single-copy transgenes *zacSi1(Psemo-1::gfp::rab-5) zacSi28(dpy-7p::eat-17d::gfp)* and *zacSi29(dpy-7p::eat-17f::gfp)*. Briefly, the donor plasmids 5’ homology arm+ *Psemo-1::gfp::rab-5 (or dpy-7p::eat-17d::gfp, or dpy-7p::eat-17f::gfp)*+ 3’ homology arm was constructed using a seamless cloning protocol. Notably, *unc-119(+)* was inserted in one of the introns of *gfp*, and several silent mutations were included to avoid recutting. The donor plasmid (50 ng/μL), *eft-3p::cas9* (50 ng/μL), *ttTi5605-sgRNA* (Addgene #47550, 50 ng/μL) and the negative selection markers *odr-1p::rfp* (30 ng/μL), *myo-2p::mcherry* (2 ng/μL), and *myo-3p::mcherry* (3 ng/μL) were mixed and injected into *unc-119(ed4)* animals. Successful single-copy knock-in animals were identified based on PCR-based genotyping and Sanger sequencing.

To generate knockout strains, a modified co-conversion protocol was used[65]. Briefly, *eft-3p::cas9* + pU6::*dpy-10sg* and 2-3 sgRNAs for the gene of interest were mixed and co-injected. To generate *eat-17(zac305)*, *eft-3p::cas9* + pU6::*dpy-10sg* (50 ng/μL, kindly provided by Dr. Suhong Xu), sgRNA#1: 5’CTTCAGCAGGAGCTCATCG3’, sgRNA#2: 5’CACGAGCGGATGTGAGTGG3’ and sgRNA#3: 5’GATCAGTTGAAAGATGAGA3’ (20 ng/μL each) were co-injected into *eat-17(ok3041); wyIs592*. Dumpy or roller F1 animals were selected and the F2 progenies were subjected to PCR-based genotyping. *zac305* contains a 496 bp deletion (flanked by 5’TCACTCGCTTCAGCAGGAGC3’ and 5’CATCCGCTCGTGCTCGTCTT3’) and 5 bp (5’AGGAG3’) insertion.

eat-17(zac276), *mec-3(zac395), mec-3(zac456)* and *mec-3(zac459)* were generated similarly. Briefly, *eft-3p::cas9* + p*U6::dpy-10 sgRNA* (50 ng/μL), *eat-17 sgRNA#1*: 5’CTTCAGCAGGAGCTCATCG3’, *eat-17 sgRNA#2*: 5’CACGAGCGGATGTGAGTGG3’, *eat-17 sgRNA#3*: 5’GATCAGTTGAAAGATGAGA3’ (20 ng/μL each) were co-injected into *wyIs587(PVD::myri-mCherry) II;wyIs50005 (Pskin::SAX-7S::gfp) X*. Dumpy or roller F1 animals were selected and the F2 progenies were subjected to PCR-based genotyping. *zac276* contains an 807 bp deletion (flanked by 5’ACACGTCGATGATTGAGCAC3’ and 5’ GAAAGATGAGAAGGAGAAGT3’) and 3 bp insertion (5’GTC3’). To generate *mec-3(zac395), Peft-3::cas9* + p*U6::dpy-10 sgRNA* (50 ng/μL), *mec-3 sgRNA#1*: 5’CTCAGTGCGATTAGTATGGTT3’, *mec-3 sgRNA#2*: 5’AAAAGTGTTTTTGGAAAAAT3’, *mec-3 sgRNA#3*: 5’ACAGATATGGTATATAAACT3’ (20 ng/μL each) were mixed and injected into *wyIs587 II; sax-7(zac311[sax-7::gfp]) IV*. Two regions were deleted in *zac395* mutants. 43 bp were deleted in the first region (flanked by 5’ ttcatttgaactATGGAAAT3’ and 5’ TCAATTGGAGTTGATCATGA3’). 371 bp were deleted in the second region (flanked by 5’ GAAAGGAGTGTCACCGACAG3’ and 5’ GCATTTATCACCGGGGGAAC3’). In addition, 21 bp (5’ AAGGAGTGTCAAGAAAGGAGT3’) were inserted into the second region. To generate *mec-3(zac456)* and *mec-3(zac459)*, the same injection mix described above was injected into *wyIs587 II; bicd-1(zac51) IV; wyIs50005 X*. 1267 bp (flanked by 5’ tagtgaaacttgtgtctaac3’ and 5’ GAATACACCAAAGCCGTCGA3’) were deleted in *zac456* mutants. 1536 bp (flanked by 5’ gatttatttcatttgaactA3’ and 5’ CGCTTATGGATACAACTTTG3’) were deleted in *zac459* mutants.

Information of the plasmids and target DNA sequences of the sgRNAs used in this study are listed in the Supplementary Table 2 and 3, respectively.

Plasmid construction

For most of the plasmid constructs used in this study, the pSM delta vector (a derivative of pPD49.26) was used as the backbone. To express genes of interest in specific tissues, *dpy-7p*(epidermis), *ser2-prom3* (PVD), *hlh-1p (muscle)*, *vha-6p* (intestine) and *semo-1p* (epidermis and intestine) were amplified from previously generated plasmids or a home-made *C. elegans* genomic DNA library. To express genes of interest at specific time points, *hsp-16.48p* was used. The coding sequences of genes of interest, such as *bicd-1* and *eat-17*, were amplified from a home-made mixed-stage *C. elegans* cDNA library. A multi-fragment cloning kit (Vazyme, ClonExpress MultiS One Step Cloning Kit, C113-02) was used to ligate the promoter, coding sequences of the target genes, coding sequences of the fluorescence protein, *unc-54 3’UTR* and the restricted enzyme-treated pSM delta vector backbone.

To generate repair donor plasmids for CRISPR/cas9-mediated homologous directed repair, ~600 bp homologous arms (5’ HA and 3’ HA) were amplified from the home-made N2 genomic DNA library. *gfp* coding sequences with floxed *unc-119(+)* sequences were amplified from pMLS252 (Addgene Plasmid #73720)[64]. One or multiple silent mutation(s) were introduced in the repair template to prevent recutting. A multi-fragment cloning kit (Vazyme, ClonExpress MultiS One Step Cloning Kit, C113-02) was used.

A PCR-based Quick-Change cloning method was used to generate plasmids to express sgRNA for the gene of interest. Briefly, a reverse primer with 5’ phosphate added and a forward primer with target sequence (19 base pairs) and part of the sgRNA scaffold were used to amplify the entire sgRNA template plasmid. The concentration of the template DNA used in the PCR reaction was as low as 0.25 ng/μL so that DpnI treatment to digest the template plasmids could be skipped. Linear PCR product was ligated by using T4 DNA ligase. The ligation product was transformed into competent cells and correct sgRNA-expressing plasmids were identified via Sanger sequencing.

Protein expression and purification

Various full length and fragments of EAT-17F, BICD-1 and Rab genes were cloned into a modified pET32a vector for protein expression. The N-terminal thioredoxin-His$_6$-tagged proteins and N-terminal MBP-His$_6$-tagged proteins were expressed in *Escherichia coli* BL21 (DE3) cells in LB mediums induced by IPTG at 16°C for 20 h and purified using Ni-NTA agarose column followed by size exclusion chromatography (Superdex 200 or Superdex 75) in the buffer containing 100 mM NaCl, 50 mM Tris, 1 mM EDTA, and 1 mM DTT at pH 7.8. The thioredoxin-His$_6$-tag and MBP-His$_6$-tag were removed by incubation with HRV 3 C protease and separated by size exclusion chromatography as needed.

Fast Protein Liquid Chromatography (FPLC) coupled with static light scattering

The analysis was carried out on an AKTA FPLC system (GE Healthcare) coupled with a static light scattering detector (miniDawn, Wyatt) and a differential refractive index detector (Optilab, Wyatt). Protein samples with concentration of ~ 70 μM were filtered and loaded into a superdex 200 increase column (GE Healthcare) equilibrated with the buffer containing 100 mM NaCl, 50 mM Tris, 1 mM EDTA, and 1 mM DTT at pH

7.8. The data were analyzed using Origin 7.0, and the molecular weight data were calculated by ASTRA6.

Isothermal titration calorimetry assay

Isothermal titration calorimetry (ITC) measurements were carried out on a VP-ITC Microcal calorimeter (Malvern) at 25°C. All proteins were in buffer containing 100 mM NaCl, 50 mM Tris, 1 mM EDTA, and 1 mM DTT at pH 7.8. Each titration point was performed by injecting a 10 μL aliquot of syringe protein into the cell at a time interval of 180 sec to ensure that the titration peak returned to the baseline. BICD C-terminal proteins (200 μM) were loaded onto the syringe and EAT-17F proteins (20 μM) were loaded in the cell. The titration data were analyzed using the program Origin 7.0 and fitted by the one-site binding model[66].

Coimmunoprecipitation

HEK-293 cells were transfected with plasmids using PEI when the cell density reached 70%. The medium was changed every 12 h, and then the cells were harvested and lysed 40 h after transfection. Whole-cell lysates were prepared in NP40 lysis buffer (P0013F, Beyotime), and the lysates were incubated with anti-Flag beads (Sigma) for 2 h at 4°C. After washing three times with lysis buffer, the beads were incubated in 2 × SDS-PAGE loading buffer for 15 min. The samples were separated by SDS-PAGE and subsequently transferred onto a PVDF membrane (Millipore, Sigma-aldrich), probed with GFP (1:1000; Proteintech), or Flag (1:2000; Proteintech) antibodies at 4°C overnight and secondary antibodies at room temperature for 1 h, and visualized with enhanced chemiluminescence (Amersham Biosciences).

RNA interference

Worms were transferred onto RNAi plates (freshly prepared NGM containing 1 mg/mL IPTG and 1 mg/mL Ampicillin) seeded with HT115 *E. coli* strains to express gene-specific double-stranded RNAs (dsRNAs) and cultured at 20 °C.

For experiments showed in Figs. 1f, 5c and Supplementary Fig. 4a, P0 animals at L4 stage were transferred onto RNAi plates seeded with HT115 *E. coli* strains, including L4440 (empty vector as a negative control) or bacteria strains expressing gene-specific dsRNAs. F1 progenies at L4 stage were transferred onto corresponding RNAi plates and 1 day-old adults (24 h post L4) were imaged and analyzed for phenotypes.

For experiments showed in Fig. 6c and Supplementary Fig. 7a, P0 animals at L4 stage were transferred onto RNAi plates seeded with L4440 or bacteria strain expressing gene-specific dsRNAs. F1 progenies at L4 post 3 h were imaged and analyzed for phenotypes.

For experiments showed in Fig. 7a, c, and e, and Supplementary Fig. 5a, animals at L2 stage were transferred onto RNAi plates seeded with L4440 or bacteria strains expressing gene-specific dsRNAs. These animals were transferred onto corresponding RNAi plates when they reached L4 stage, and imaged and analyzed at 1 day-old adult stage.

For experiments showed in Supplementary Figs. 8c, 9a and c, P0 animals at L4 stage were transferred onto RNAi plates seeded with L4440 or bacteria strains expressing gene-specific dsRNAs. L4 stage-F1 progenies were subjected to heat shock and imaged and analyzed for phenotypes after recover for 3–6 h.

Heat shock treatment

For experiments showed in Fig. 3e, 30 worms at 1DOA stage were transferred onto NGM plates seeded with OP50, and were removed 2 h later to obtain a small-scale synchronized worm population. Based on the gonad development phenotype, it roughly takes 13 h (post egg-laying) for the animals to reach early-L1 stage; 26 h to reach early-L2 stage; 37 h to reach early-L3 stage; 49 h to reach early-L4 stage. 1 day-old adult is defined as 24 h post L4 stage. Worms at distinct developmental stages (L1, L2, L3, L4 and 1 DOA) were heat-shocked at 33°C for 1 h using a water bath. The animals were then transferred into a 20°C incubator to recover from heat-shock. Animals at the 2 day-old adult stage (24 h post 1DOA stage) were imaged and quantified for dendrite branching phenotypes.

For experiments showed in Supplementary Figs. 8c, 9a and 9b, L4-stage animals were heat-shocked at 33°C for 1 h using a water bath. The animals were then transferred into a 20°C incubator to recover from heat-shock, and then imaged and quantified for phenotypes 3–6 h post heat-shock.

Confocal imaging of *C. elegans*

C. elegans were immobilized on 2% agar pads using 10 mM levamisole in M9 buffer. All confocal images in this study were acquired on an Olympus IX83 fluorescence microscope equipped with a spinning-disk confocal scanner (Yokogawa CSU-W1), 10X/ 20X/ 40X magnification, a 60× NA 1.49 oil Apochromat objective, an sCMOS camera (Prime 95B), 488/561 nm lasers (OBIS) and a PIEZO stage (ASI). All confocal images were acquired using a 60×359 objective. For results showed in Figs. 1f, 2a, 3a, 3b, 3e, 4a, 4d, 5e, 7a, and Supplementary Figs. 1a, 2b, 3b, 4a, 4d, 5a and 10c, z-stacks with 0.8 μm -1 μm step size were obtained, and the maximum intensity of projections were shown. For results showed in Figs. 5a, 6c and Supplementary Fig. 6a, z-stacks with 0.8 μm step size were captured and proper single-focal-plane images were showed. For results showed in Figs. 5a, 5c, 6a, 6c, 7c, 7e, and Supplementary Figs. 2a, 7a, 8c, 9a and 9c, single-focal-plane images were obtained and showed.

Snapshot-based analysis of PVD dendrite morphogenesis

1°, 2°, 3°, 4° dendrites are defined as previously described[19] and showed in Fig. 1a (in green) and 1 G (in black). The branches that do not belong to the above-mentioned regular 1°, 2°, 3°, 4° dendrites are defined as ectopic branches, as showed in Fig. 1g (in red). To quantify the dendrite branching phenotypes, numbers of 1°, 2°, 3°, 4° branches and ectopic branches in a 100 μm region anterior to the PVD cell body were quantified manually.

Time-lapse imaging and analysis of dendrite formation

Animals at L4 stage were recognized and picked based on the crescent shape in the middle of the worm body. About 3 h later, these animals were anesthetized with 10 mM levamisole and subjected to imaging using a protocol developed by Chai et al.[67]. Z-stacks were taken every 2 min (exposure time: 100 ms) for 2 h. The outgrowth speed, retraction speed, number of outgrowth events and retraction events of ectopic branches were analyzed manually using image J. 10 animals were quantified for each strain.

Quantification of the fluorescence intensity of SAX-7 signals

For experiments showed in Fig. 5a and Supplementary Fig. 6a, animals at 12 h post L4 stage were imaged and the SAX-7::GFP intensity in the epidermis were quantified. For experiments showed in Supplementary Fig. 8c, heat shock-treated animals were imaged and the SAX-7::mCH intensity at the sublateral 3° lines were quantified. For each animal, 5 region-of-interest were randomly selected and the mean fluorescence intensity was quantified using Image J. The background signal outside of the animals was subtracted.

For experiments showed in Supplementary Fig. 9a and 9c, heat shock treated-animals were imaged and the SAX-7::mCherry intensity within endosomes or lysosomes (labeled by RME-8::GFP and SCAV-3::GFP, respectively) was quantified. For each animal, 400 μm^2 were randomly selected and the total fluorescence intensity was quantified using Image J. The background signal outside of the animals was subtracted.

Quantification of % SAX-7-positive endosomes and lysosomes

For experiments showed in Fig. 6a, animals at 1DOA were imaged and the percentage of early endosomes and late endosomes/ lysosomes with SAX-7::mCherry in their lumen was quantified. 20 animals were quantified for each strain.

For experiments showed in Fig. 6c and Supplementary Fig. 7a, 3h-post L4 stage-animals were imaged and the percentage of early endosomes (labeled by YFP::2xFYVE or RME-8::GFP) with SAX-7::mCherry in their lumen was quantified. 20 animals were quantified for each strain.

Quantification of number of early endosomes in epidermis

To quantify number of RAB-5, 2xFYVE and RME-8-labeled early endosomes, 1 day-old adults were imaged. A region of interest (95.036 μm^2) was randomly selected for each animal and the number of vesicles within this area was manually counted.

Locomotion assay

A locomotion assay was performed following the protocol as previously described[47]. 10–20 worms at 1 day-old stage were individually transferred onto freshly prepared NGM plates, and then the plates were put in a 20 °C incubator for 2 h. The crawling tracks were imaged using a Nikon SM218 stereo microscope with a 1x SHR Plan Apo objective (NA: 0.15). The trajectory's amplitude (the distance between opposite peaks) and wavelength (the distance between two successive peaks) were measured using Image J. For each animal, 10–15 regions (583.66 µm x 583.66 µm for each region) were randomly chosen and imaged. 50 amplitude or wavelength were quantified for each animal.

Western blotting analysis for *C. elegans* proteins

To detect the expression of the long and short isoforms of the endogenous EAT-17 proteins, *N2*, *eat-17(zac345[eat-17::GFP])*, *eat-17(zac645[eat-17(ok2928)::GFP])*, *eat-17(zac647[eat-17(ok3041)::GFP])* and *eat-17(zac649[eat-17(ok2983)::GFP])* animals were synchronized using a bleach buffer-based protocol and grew in 15–20 6 cm-NGM plates seeded with OP50. Animals were harvested when they reached 1DOA stage by washing with M9 buffer for 3 times, centrifuged to remove the supernatant, freezed-and-thawed with liquid nitrogen twice, and then placed onto ice.

To detect the expression of SAX-7 in epidermis, *(1) wyIs587; wyIs50005, (2) eat-17(zac276); wyIs587; wyIs50005, (3) bicd-1(zac51); wyIs587; wyIs50005, (4) L4440 RNAi; wyIs587; wyIs50005* and (5) *rab-5 RNAi; wyIs587; wyIs50005* animals were synchronized using a bleach buffer-based protocol and grew in 15-20 6-cm NGM plates seeded with OP50 (for 1-3) or HT115 (for 4-5). 12 h post L4 stage-animals were harvested by washing with M9 buffer for 3 times, centrifuged to remove the supernatant, freezed-and-thawed with liquid nitrogen twice, and then placed onto ice.

150 µL of protein lysate buffer (TAP/protease inhibitor ratio 200:1, Bimake) was added into each worm sample. After grinding with a grinding pestle on ice for 40 min, pass liquid nitrogen every 5 min, the samples were centrifuged at 15000 rpm at 4°C for 20 min, and then the supernatant was transferred into a new 1.5 mL EP tube and 5x loading buffer was added. The samples were then boiled at 95°C for 10 min. Proteins were detected using Western blotting. The following antibodies were used: mouse monoclonal anti-GFP (1:4000, EarthOx), anti-tubulin (1:5000, Sigma-Aldrich) and secondary antibody goat anti mouse (1:8000, EarthOx).

Statistical analysis

Data were analyzed using Prism (GraphPad). These values were showed as mean ± s.e.m. One-way or two-way analysis of variance (ANOVA) was performed, followed by Tukey's post-test to statistically compare multiple sets of samples. The two-tailed unpaired student's *t*-test was used to determine statistically significant differences between the two groups. For all quantifications, *P*-values were reported for each statistical test, where $^{*}P < 0.05$, $^{**}P < 0.01$, $^{***}P < 0.001$, $^{****}P < 0.0001$ and ns were not significant ($P > 0.05$).

Reporting summary

Further information on research design is available in the Nature Portfolio Reporting Summary linked to this article.

Data availability

The full raw data that support the results of this study are available upon request. Source data are provided with this paper.

References

1. Jan, Y. N. & Jan, L. Y. Branching out: mechanisms of dendritic arborization (vol 11, pg 316, 2010). *Nat. Re v. Neurosci.* **11**, 316–328 (2010).
2. Dong, X. T., Shen, K. & Bulow, H. E. Intrinsic and extrinsic mechanisms of dendritic morphogenesis. *Annu Rev. Physiol.* **77**, 271–300 (2015).
3. Lefebvre, J. L. Molecular mechanisms that mediate dendrite morphogenesis. *Curr. Top. Dev. Biol.* **142**, 233–282 (2021).
4. Sundararajan, L., Stern, J. & Miller, D. M. Mechanisms that regulate morphogenesis of a highly branched neuron in C. elegans. *Dev. Biol.* **451**, 53–67 (2019).
5. Inberg, S. et al. Lessons from worm dendritic patterning. *Annu Rev. Neurosci.* **42**, 365 (2019).
6. Lee, T. M., Winter, C., Marticke, S. S., Lee, A. & Luo, L. Q. Essential roles of drosophila RhoA in the regulation of neuroblast proliferation and dendritic but not axonal morphogenesis. *Neuron* **25**, 307–316 (2000).
7. Yasunaga, K. et al. Adult Drosophila sensory neurons specify dendritic territories independently of dendritic contacts through the Wnt5-Drl signaling pathway. *Genes Dev.* **29**, 1763–1775 (2015).
8. Lanoue, V. et al. The Wnt receptor Ryk is a negative regulator of mammalian dendrite morphogenesis. *Sci. Rep.-Uk* **7**, 5965 (2017).
9. Emoto, K. et al. Control of dendritic branching and tiling by the tricornered-kinase/furry signaling pathway in Drosophila sensory neurons. *Cell* **119**, 245–256 (2004).
10. Albeg, A. et al. C-elegans multi-dendritic sensory neurons: morphology and function. *Mol. Cell Neurosci.* **46**, 308–317 (2011).
11. Dong, X. T., Liu, O. W., Howell, A. S. & Shen, K. An extracellular adhesion molecule complex patterns dendritic branching and morphogenesis. *Cell* **155**, 296–307 (2013).
12. Liu, O. W. & Shen, K. The transmembrane LRR protein DMA-1 promotes dendrite branching and growth in C. elegans. *Nat. Neurosci.* **15**, 57–U74 (2012).
13. Salzberg, Y. et al. Skin-derived cues control arborization of sensory dendrites in caenorhabditis elegans. *Cell* **155**, 308–320 (2013).
14. Zou, W. et al. A multi-protein receptor-ligand complex underlies combinatorial dendrite guidance choices in C. elegans. *Elife* **5**, e18345 (2016).
15. Diaz-Balzac, C. A. et al. Muscle- and skin-derived cues jointly orchestrate patterning of somatosensory dendrites (vol 26, pg 2379, 2016). *Curr. Biol.* **26**, 2397–2397 (2016).
16. Smith, C. J. et al. Sensory neuron fates are distinguished by a transcriptional switch that regulates dendrite branch stabilization. *Neuron* **79**, 266–280 (2013).
17. Zou, W. et al. A dendritic guidance receptor complex brings together distinct actin regulators to drive efficient F-actin assembly and branching. *Dev. Cell* **45**, 362 (2018).
18. Tang, L. T. H. et al. TIAM-1/GEF can shape somatosensory dendrites independently of its GEF activity by regulating F-actin localization. *Elife* **8**, e38949 (2019).
19. Zou, W., Yadav, S., DeVault, L., Jan, Y. N. & Sherwood, D. R. RAB-10-dependent membrane transport is required for dendrite arborization. *PLoS Genet* **11**, e1005484 (2015).
20. Taylor, C. A., Yan, J., Howell, A. S., Dong, X. T. & Shen, K. RAB-10 regulates dendritic branching by balancing dendritic transport. *PLoS Genet* **11**, e1005695 (2015).

21. Wei, X. et al. The unfolded protein response is required for dendrite morphogenesis. *Elife* **4**, e06963 (2015).
22. Salzberg, Y. et al. Reduced insulin/insulin-like growth factor receptor signaling mitigates defective dendrite morphogenesis in mutants of the ER stress sensor IRE-1. *Plos Genet* **13**, e1006579 (2017).
23. Dong, X. T. et al. Precise regulation of the guidance receptor DMA-1 by KPC-1/Furin instructs dendritic branching decisions. *Elife* **5**, e11008 (2016).
24. Liang, X., Dong, X. T., Moerman, D. G., Shen, K. & Wang, X. M. Sarcomeres pattern proprioceptive sensory dendritic endings through UNC-52/perlecan in C. elegans. *Dev. Cell* **33**, 388–400 (2015).
25. Sasidharan, N. et al. RAB-5 and RAB-10 cooperate to regulate neuropeptide release in Caenorhabditis elegans. *Proc. Natl Acad. Sci. USA* **109**, 18944–18949 (2012).
26. Roach, N. P. et al. The full-length transcriptome of C. elegans using direct RNA sequencing. *Genome Res.* **30**, 299–312 (2020).
27. Sternberg, P. W. et al. WormBase 2024: status and transitioning to alliance infrastructure. *Genetics* **227**, iyae050 (2024).
28. Straud, S., Lee, I., Song, B. M., Avery, L. & You, Y. J. The jaw of the worm: GTPase-activating protein EAT-17 regulates grinder formation in caenorhabditis elegans. *Genetics* **195**, 115 (2013).
29. Dickinson, D. J., Ward, J. D., Reiner, D. J. & Goldstein, B. Engineering the Caenorhabditis elegans genome using Cas9-triggered homologous recombination. *Nat. Methods* **10**, 1028 (2013).
30. Tsalik, E. L. et al. LIM homeobox gene-dependent expression of biogenic amine receptors in restricted regions of the C-elegans nervous system. *Dev. Biol.* **263**, 81–102 (2003).
31. Chen, L., Krause, M., Draper, B., Weintraub, H. & Fire, A. Body-wall muscle formation in caenorhabditis-elegans embryos that lack the myod homolog Hlh-1. *Science* **256**, 240–243 (1992).
32. Gilleard, J. S., Barry, J. D. & Johnstone, I. L. cis regulatory requirements for hypodermal cell-specific expression of the caenorhabditis elegans cuticle collagen gene dpy-7. *Mol. Cell Biol.* **17**, 2301–2311 (1997).
33. Aguirre-Chen, C., Bulow, H. E. & Kaprielian, Z. C. elegans bicd-1, homolog of the Drosophila dynein accessory factor Bicaudal D, regulates the branching of PVD sensory neuron dendrites. *Development* **138**, 507–518 (2011).
34. Zhu, T., Liang, X., Wang, X. M. & Shen, K. Dynein and EFF-1 control dendrite morphology by regulating the localization pattern of SAX-7 in epidermal cells. *J. Cell Sci.* **130**, 4063–4071 (2017).
35. Smith, C. J. et al. Time-lapse imaging and cell-specific expression profiling reveal dynamic branching and molecular determinants of a multi-dendritic nociceptor in C. elegans. *Dev. Biol.* **345**, 18–33 (2010).
36. Zou, W. et al. Caenorhabditis elegans myotubularin MTM-1 negatively regulates the engulfment of apoptotic cells. *PLoS Genet* **5**, e1000679 (2009).
37. Mauvezin, C., Nagy, P., Juhász, G. & Neufeld, T. P. Autophagosome-lysosome fusion is independent of V-ATPase-mediated acidification. *Nat. Commun.* **6**, 7007 (2015).
38. Chen, C. C. et al. RAB-10 is required for endocytic recycling in the Caenorhabditis elegans intestine. *Mol. Biol. Cell* **17**, 1286–1297 (2006).
39. Kinchen, J. M. et al. A pathway for phagosome maturation during engulfment of apoptotic cells. *Nat. Cell Biol.* **10**, 556–566 (2008).
40. Zhang, Y., Grant, B. & Hirsh, D. RME-8, a conserved J-domain protein, is required for endocytosis in Caenorhabditis elegans. *Mol. Biol. Cell* **12**, 2011–2021 (2001).
41. Norris, A. et al. SNX-1 and RME-8 oppose the assembly of HGRS-1/ESCRT-0 degradative microdomains on endosomes. *Proc. Natl Acad. Sci. USA* **114**, E307–e316 (2017).
42. Li, Y. et al. The lysosomal membrane protein SCAV-3 maintains lysosome integrity and adult longevity. *J. Cell Biol.* **215**, 167–185 (2016).
43. Driesschaert, B., Mergan, L. & Temmerman, L. Conditional gene expression in invertebrate animal models. *J. Genet Genom.* **48**, 14–31 (2021).
44. Grant, B. & Hirsh, D. Receptor-mediated endocytosis in the Caenorhabditis elegans oocyte. *Mol. Biol. Cell* **10**, 4311–4326 (1999).
45. Fang, J. et al. Ribo-on and Ribo-off tools using a self-cleaving ribozyme allow manipulation of endogenous gene expression in C. elegans. *Commun. Biol.* **6**, 816 (2023).
46. Shen, Z. F. et al. Conditional knockouts generated by engineered CRISPR-Cas9 endonuclease reveal the roles of coronin in C. elegans neural development. *Dev. Cell* **30**, 625–636 (2014).
47. Tao, L. et al. Parallel processing of two mechanosensory modalities by a single neuron in C. elegans. *Dev. Cell* **51**, 617 (2019).
48. Satoh, D. et al. Spatial control of branching within dendritic arbors by dynein-dependent transport of Rab5-endosomes. *Nat. Cell Biol.* **10**, 1164–1171 (2008).
49. Yang, W. K. et al. Nak regulates localization of clathrin sites in higher-order dendrites to promote local dendrite growth. *Neuron* **72**, 285–299 (2011).
50. Kanamori, T., Yoshino, J., Yasunaga, K., Dairyo, Y. & Emoto, K. Local endocytosis triggers dendritic thinning and pruning in Drosophila sensory neurons. *Nat. Commun.* **6**, 6515 (2015).
51. Zhang, H. et al. Endocytic pathways downregulate the L1-type cell adhesion molecule neuroglian to promote dendrite pruning in Drosophila. *Dev. Cell* **30**, 463–478 (2014).
52. Dabbeekeh, J. T. S., Faitar, S. L., Dufresne, C. P. & Cowell, J. K. The EVI5 TBC domain provides the GTPase-activating protein motif for RAB11. *Oncogene* **26**, 2804–2808 (2007).
53. Laflamme, C. et al. Evi5 promotes collective cell migration through its Rab-GAP activity. *J. Cell Biol.* **198**, 57–67 (2012).
54. Westlake, C. J. et al. Identification of Rab11 as a small GTPase binding protein for the Evi5 oncogene. *Proc. Natl Acad. Sci. USA* **104**, 1236–1241 (2007).
55. McKenney, R. J., Huynh, W., Tanenbaum, M. E., Bhabha, G. & Vale, R. D. Activation of cytoplasmic dynein motility by dynactin-cargo adapter complexes. *Science* **345**, 337–341 (2014).
56. Matanis, T. et al. Bicaudal-D regulates COPI-independent golgi-ER transport by recruiting the dynein-dynactin motor complex. *Nat. Cell Biol.* **4**, 986–992 (2002).
57. Short, B., Preisinger, C., Schaletzky, J., Kopajtich, R. & Barr, F. A. The Rab6 GTPase regulates recruitment of the dynactin complex to golgi membranes. *Curr. Biol.* **12**, 1792–U1795 (2002).
58. Splinter, D. et al. BICD2, dynactin, and LIS1 cooperate in regulating dynein recruitment to cellular structures. *Mol. Biol. Cell* **23**, 4226–4241 (2012).
59. Hoogenraad, C. C. et al. Mammalian golgi-associated bicaudal-D2 functions in the dynein-dynactin pathway by interacting with these complexes. *Embo J.* **20**, 4041–4054 (2001).
60. Terawaki, S., Yoshikane, A., Higuchi, Y. & Wakamatsu, K. Structural basis for cargo binding and autoinhibition of bicaudal-D1 by a parallel coiled-coil with homotypic registry. *Biochem. Bioph. Res. Co.* **460**, 451–456 (2015).
61. Brenner, S. The genetics of Caenorhabditis elegans. *Genetics* **77**, 71–94 (1974).
62. Davis, M. W. et al. Rapid single nucleotide polymorphism mapping in C-elegans. *Bmc Genom.* **6**, 118 (2005).
63. Minevich, G., Park, D. S., Blankenberg, D., Poole, R. J. & Hobert, O. CloudMap: A cloud-based pipeline for analysis of mutant genome sequences. *Genetics* **192**, 1249 (2012).
64. Schwartz, M. L. & Jorgensen, E. M. SapTrap, a toolkit for high-throughput CRISPR/Cas9 gene modification in Caenorhabditis elegans. *Genetics* **202**, 1277 (2016).

65. Arribere, J. A. et al. Efficient marker-free recovery of custom genetic modifications with CRISPR/Cas9 in Caenorhabditis elegans. *Genetics* **198**, 837–842 (2014).
66. Ye, J. et al. Structural basis of GABARAP-mediated GABA(A) receptor trafficking and functions on GABAergic synaptic transmission. *Nat. Commun*. **12**, 297 (2021).
67. Chai, Y. P. et al. Live imaging of cellular dynamics during Caenorhabditis elegans postembryonic development. *Nat. Protoc*. **7**, 2090–2102 (2012).

Acknowledgements

We thank Drs. Kang Shen (Stanford University), Xiaochen Wang (Southern University of Science and Technology), Hui Xiao (Shaanxi Normal University), Hongyun Tang (Westlake University), Daniel J Dickinson (UT Austin), Erik M. Jorgensen (University of Utah), Suhong Xu (Zhejiang University) and Lijun Kang (Zhejiang University) for sharing reagents and/or equipment. This work was supported by the National Natural Science Foundation of China grants 31800861, 31970919 and 32370822, (to W.Zou), 32170767 and 22122703 (to C.W.). Some strains were provided by the CGC, which is funded by NIH Office of Research Infrastructure Programs (P40 OD010440), and the MITANI Lab through the National Bio-Resource Project of the MEXT, Japan.

Author contributions

W.Zou and C.W. conceived and supervised the project, designed the experiments, and analyzed the data. J.F. and W.Zhao performed most of the *C. elegans* experiments. W.J. performed the biochemical experiments showed in Fig. 4. J.W., B.Cao and N.W. generated some reagents or helped with phenotypic quantifications. W.Zou, C.W. and B.Chen wrote and revised the manuscript with input from all authors.

Competing interests

The authors declare no competing interests.

Additional information

Supplementary information The online version contains supplementary material available at https://doi.org/10.1038/s41467-024-53970-3.

Correspondence and requests for materials should be addressed to Chao Wang or Wei Zou.

Peer review information *Nature Communications* thanks Cheng-Ting Chien and the other, anonymous, reviewer(s) for their contribution to the peer review of this work. A peer review file is available.

Reprints and permissions information is available at http://www.nature.com/reprints